Magnitudes of Induced Earthquakes in Low-Stress Environments

by J. Maurer and P. Segall

Abstract   An outstanding question for predicting hazard from induced seismicity is what controls the size distribution of events. For injection-induced seismicity, ruptures may be confined to the region of perturbed stress and pore pressure when the background ratio of shear to normal stress is low. We explore the distribution of earthquake magnitudes under the restrictive assumption that no events occur outside the stress-perturbed region around the injector. We derive mathematical expressions for the instantaneous distribution of earthquake magnitudes given a volume-averaged seismicity rate, growth rate of the perturbed region, and background fault-size distribution, assuming the latter follows a truncated Gutenberg–Richter distribution (GRD). The distribution of magnitudes can be written as the sum of three terms: faults fully inside the region, partially inside, and faults fully covering the region. The predicted frequency–magnitude distribution shows time-dependent changes relative to the GRD. These depend on the ratio of largest fault size to the (time-dependent) radius of the perturbed region and the b-value. The largest magnitude event is the smaller of either the perturbed region or largest fault size present, and in some simulations is observed post shut-in due to the high rate of events just after shut-in coupled with the continued growth of the perturbed region.

Introduction

Induced and triggered seismicity has been a growing problem in the central United States in recent years. This provides both challenges and opportunities to learn about the nature of earthquakes. From a hazards perspective, an important goal is to forecast the rate, magnitudes, and spatial distribution of induced earthquakes for a given injection scenario (e.g., Király-Proag et al., 2016). Several studies have previously modeled the number of events induced by injection (e.g., Deichmann and Giardini, 2009; Bachmann et al., 2011; Hakimhashemi et al., 2014; Dieterich et al., 2015; Segall and Lu, 2015). Estimating the hazard from induced earthquakes requires knowledge of the rate of earthquake activity and the frequency–magnitude distribution (FMD) of induced events, as well as the rate at which shaking decays with distance from the sources (via ground-motion prediction equations) (e.g., Atkinson et al., 2015).

A central question in the study of injection-induced seismicity is whether the rupture length and hence magnitude of triggered earthquakes is in some way restricted by the injection process, or is solely determined by geologic factors such as the size of faults and the distribution of tectonic stress. Specifically, will an induced earthquake be restricted to the region around the injector with relatively high pore pressure? Alternatively, will an earthquake once induced rupture and grow in the same manner as natural earthquakes? Some studies suggested that the largest earthquake magnitude is controlled in some way by the volume of injected fluid (e.g.,

Baisch et al., 2010; Shapiro et al., 2011, 2013; McGarr, 2014; Dieterich et al., 2015). In contrast, van der Elst et al. (2016) argue that the volume of injection controls the total number of events, whereas the largest magnitude is that expected from the Gutenberg–Richter distribution (GRD) given the observed earthquake rate. Resolving this issue and more generally understanding the factors that control the FMD of triggered earthquakes is an important challenge in induced seismicity.

Relative to this question, a number of numerical earthquake rupture simulations show that once nucleated, the extent of rupture depends on local stress heterogeneity, fault geometry, and critically, the ratio of the average background shear to effective normal stress (e.g., Fang and Dunham, 2013; Dieterich et al., 2015; Schmitt et al., 2015). When the shear to effective normal stress ratio is sufficiently high, ruptures are self-sustaining (i.e., limited only by the size of the fault), whereas for lower ratios, ruptures may self-arrest after propagating some distance (Dunham et al., 2011; Fang and Dunham, 2013; Schmitt et al., 2015). For low-stress environments, it is likely that induced earthquakes are limited by the volume of crust perturbed by injection, in contrast to high-stress environments where triggered earthquakes are likely to be limited by the same factors that control the size distribution of natural earthquakes (see also Shapiro, 2015, section 5.2.7). The simulations of Dieterich et al. (2015) are consistent with this behavior, showing a tendency for

ruptures to arrest where the perturbing pore-pressure drops below a threshold that depends on the background shear stress level. In this study, we explore analytically the hypothesis that induced ruptures are restricted to a stress and pore-pressure-perturbed volume of crust, as might be appropriate in a low shear stress environment, using an analytical approach. We adopt a highly idealized, end-member model of injection and the perturbed stress volume to permit analytical solutions. In this simplification, earthquakes cannot nucleate or rupture outside the stress-perturbed region, which we take to be spherical with radius that grows with time due to pore-pressure and poroelastic stress diffusion. We derive expressions for the time-dependent FMDs that result from this scenario and consider whether it is possible to distinguish between these and the GRD.

It should be emphasized that this is a highly idealized end-member model that cannot capture all of the effects that come into play during injection and earthquake nucleation, propagation, and arrest. However, we find interesting and even unexpected results that should be informative for understanding more realistic and complex models. The restriction of seismicity to a region around the injector alters the relative proportions of small- to large-magnitude events in different ways at different times during the injection sequence. We anticipate this model could be used to inform more detailed studies of earthquake magnitudes occurring in injection-induced sequences.

Model and Methods

Background

Segall–Lu 2015 Model. This study builds on the work of Segall and Lu (2015), who considered an idealized model of a point source of injection in a poroelastic full space. They employed the seismicity rate model of Dieterich (1994) to relate changes in Coulomb stress to the rate of earthquake nucleations, assuming that a uniform tectonic loading would result in a constant rate of events. Because the Dieterich (1994) theory does not predict magnitude, they developed a simple end-member conceptual model to determine earthquake magnitudes. Faults were assumed to be circular cracks of constant strike and dip, and spatially uniform density. The rate of nucleations, which could occur anywhere inside the perturbed region, was provided by the Dietrich model given the poroelastic changes in stress and pore pressure. They assumed that at some distance proportional to $\sqrt{Dt}$, in which D is hydraulic diffusivity, the background shear stress was too low for ruptures to propagate outside of the perturbed volume.

Considering crack-like sources with radius ρ, Segall and Lu (2015) write the rate of magnitude M_w events $R(M_w, t)$ as

$$R(M_w, t) = \bar{R}(t)G(\rho(M_w); b)P_{in}(\rho(M_w), t), \quad (1)$$

in which $\bar{R}(t)$ is the volume-integrated rate of earthquake nucleations, $G(\rho; b)$ is the probability that a nucleation occurs on a fault of size ρ, corresponding to magnitude

M_w (assumed to follow the GRD, with b-value b), and P_{in} describes the probability that a source with radius ρ is completely contained within the perturbed region, given that it intersects the region.

Their simple model is based on the following assumptions:

1. The radius of the injection-perturbed region, assumed spherical with volume V, grows proportionally to $\sqrt{ct}$.
2. The fault-size distribution is such that, absent perturbations due to injection, tectonic loading would result in a GRD of event magnitudes.
3. Earthquake nucleations are limited to the perturbed volume V around the injector.
4. Earthquakes, once they nucleate, rupture the entire fault.
5. The background shear-to-normal stress ratio is low such that ruptures can only occur inside V.
6. As a consequence of the previous two assumptions, only faults located fully inside the stress-perturbed region host earthquakes.

The last assumption implies that the probability of a nucleation evolving into a magnitude M_w event is independent of location as long as the source is fully contained within the perturbed zone.

Shapiro et al. Model. Our study also relates to work by Shapiro and others (Shapiro *et al.*, 2011, 2013; Shapiro, 2015, we refer to this set of publications collectively as "Shapiro *et al.*"). They adopt the first four assumptions listed above, although not in the context of low background stress. They provide a basis for thinking of the perturbed region as a finite volume, even though the pore pressure smoothly decays with distance from the injector. They assume a minimum stress perturbation is needed to initiate failure, and thus the size of the perturbed volume is given by the point at which the pore pressure reaches this minimum threshold for nucleation.

Shapiro *et al.* consider how the finiteness of the perturbed region affects the distribution of earthquake magnitudes. The approach is to assume that nucleations are limited to the stress-perturbed volume, but that once nucleated, earthquakes rupture the entire fault. They write the size distribution of events as a factor modifying the GRD to account for the influence of the perturbed region

$$P_{event}(\rho) = G_{stim}(\rho)G(\rho; b), \quad (2)$$

in which G_{stim} ($G_w(X)$ in Shapiro, 2015) is a factor (not a probability; see the Appendix) that describes whether or not a fault intersecting the perturbed region is sufficiently stimulated to produce an event. Shapiro *et al.* write this as

$$G_{stim}(\rho) = P_s(\rho)/P_c(\rho).$$

$P_c(\rho)$ is the conditional probability that the center of a fault (with radius ρ) is inside the perturbed region V, given that the

fault at least intersects V. Under these assumptions, $G(\rho; b)$ applies to fault centers. Thus, $G(\rho; b)/P_c(\rho)$ (for $\rho > 0$) is proportional to the probability distribution of fault sizes ρ intersecting the perturbed region.

P_s is the probability that the fault is sufficiently stimulated to produce an event. Shapiro *et al.* suggest two end-member models that bound this probability. The first is that faults must be fully contained inside the perturbed region to host an event, as in Segall and Lu (2015). Under this condition, $P_s = P_{\text{vol}} P_c$, in which P_{vol} is the probability that a fault is fully contained within V, conditioned on its center being inside V. This results in $G_{\text{stim}} = P_{\text{vol}}$ and

$$P_{\text{event}}(\rho) = P_{\text{vol}}(\rho) G(\rho). \qquad (3)$$

The expressions given by Shapiro *et al.* to compute $P_s = P_{\text{vol}} P_c$ are identical within a normalizing constant to Segall and Lu (2015) (see equation 5.52 with 5.91 in Shapiro, 2015; or equation 2 in Shapiro *et al.*, 2011, with equation A7 in Shapiro *et al.*, 2013, compare to Segall and Lu, 2015, equation C2) and equation (20) in this study. This is not necessarily expected because Shapiro *et al.* derive their model for arbitrary fault orientations. In addition, their formulation appears to conflict with that of Segall and Lu (2015), because equation (3) is not the same as P_{in} given by Segall and Lu (2015). The difference may be understood by noting that multiplying P_{vol} by P_c scales the probability, so that in the limit that the event size goes to zero, the probability goes to one, and in the limit as the event size goes to the maximum, corresponding to $a(t)$, the probability approaches zero. Dividing P_s by P_c simply rescales the probabilities. Thus, the two formulations are consistent.

In the second end-member model considered by Shapiro *et al.*, any fault with even an infinitesimal fraction inside V produces an event of that size. This requires that $P_s = 1$, so $G_{\text{stim}} = 1/P_c$. Because this is the same as the distribution of faults intersecting V, it results in more events at every magnitude than GRD. An intermediate case is that some representative fraction of the fault needs to be contained within V to result in a rupture, for example, the center, which results in ordinary GRD. All of these scenarios assume that a particular source either hosts an earthquake or it does not; partially ruptured sources are not considered.

Shapiro *et al.* only consider full-fault ruptures; they have not explored the case in which earthquake ruptures are confined to the perturbed volume V. Their lower-bound scenario does restrict all events to V, but under the restrictive assumption that the entire fault must be contained within the region. It could be possible for a rupture to begin to grow inside V, then arrest when encountering an increase in strength at the edge of the region. This might be the case in areas of low background stress, where the perturbation due to injection is sufficient to cause nucleation and rupture inside the perturbed zone, but there is insufficient stress outside the zone for rupture to continue. It is this case of partial ruptures that we investigate in this study.
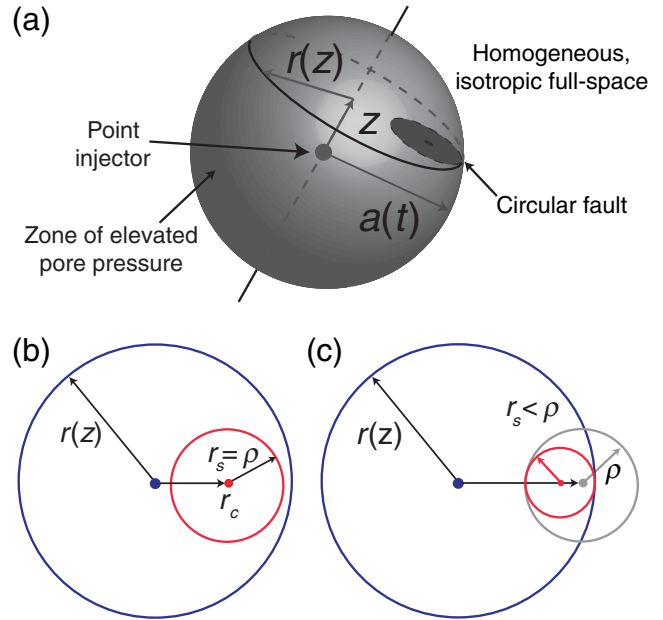
Figure 1. (a) Basic geometry of the model. The perturbed region is represented as a sphere with radius $a(t) \propto \sqrt{t}$, with the z axis perpendicular to circular crack-like faults of constant orientation. Denote $r(z)$ as the cross-sectional radius of the sphere at a given z. (b) A cross-sectional view, with a single fault with radius ρ located a distance r_c from the center of the circle. The earthquake will have radius $r_s = \rho$, because the fault is completely inside the perturbed region. (c) A fault of the same size as in (b), but in this case located only partially inside the sphere, so the earthquake radius r_s will be less than ρ. The color version of this figure is available only in the electronic edition.

Method

In this study, we use the idealized geometry of Segall and Lu (2015) to simplify analysis of the complete probabilistic distribution of event sizes as a function of time. Figure 1a shows the geometry used to simulate earthquake magnitudes. We assume injection at a point in a full-space with homogeneous and isotropic properties. No events occur outside of the local region perturbed by injection, which is assumed to be spherical with radius $a(t)$ and cross-sectional radius $r(z)$ (Fig. 1). Diffusive processes lead to a gradual decrease in pore pressure and stress with distance from the injector; here, we model the transition from stresses high enough to allow dynamic rupture to those too low as a hard boundary for mathematical tractability, which is a strong simplification. We will show that this rather artificial cutoff leads to some interesting behavior under certain conditions.

All faults have the same unit normal, which we take without loss of generality to be parallel to the z axis. Earthquakes are modeled as circular ruptures with radius r_s, occurring on circular faults with radius ρ. The location of the center of a fault hosting an earthquake is denoted by r_c. Again for simplicity, we make the assumption that no events nucleate or propagate outside the spherical stress-perturbed region with radius that grows in time since injection. Segall

and Lu (2015) restricted their analysis to faults that lie completely within the region of elevated pore pressure (Fig. 1b), neglecting faults that are only partially inside (Fig. 1c). Here, we include these partial ruptures (in an idealized fashion) in modeling the earthquake-size distribution.

Figure 1b shows an example in which the fault and earthquake sizes are identical (i.e., $r_s = \rho$), because the fault is completely inside the spherical perturbed region. Figure 1c shows a second case in which the fault is larger than the induced earthquake because it is only partially within the perturbed region. For simplicity, the partial ruptures are modeled as the largest circle on the fault inscribed within the perturbed region with radius $r(z)$. The two faults in (b) and (c) are the same size, but because of the differences in their locations relative to the injection point they end up hosting earthquakes of different sizes. Events can be as large as the hosting fault, but may be smaller. Faults located completely outside the perturbed region do not host earthquakes.

Based on the above assumptions, we express the general form for the total rate of earthquakes in time and magnitude $R(M_w, t)$ in the following form:

$$R(M_w, t) = \int_V R(\mathbf{x}, t) P(M_w | \mathbf{x}, t) dV, \qquad (4)$$

in which $R(\mathbf{x}, t)$ is the rate of earthquake nucleations as a function of space and time, and $P(M_w | \mathbf{x}, t)$ is the conditional probability that a nucleation at location $\mathbf{x}$ and time t will give rise to a magnitude M_w event. The volume integral is over the region of crust where the stress and pore pressure has been sufficiently perturbed to induce events, which we approximate as a sphere with radius proportional to $a(t) \propto \sqrt{ct}$.

Expressing equation (4) as a function of event radii r_s instead of magnitude:

$$R(M_w, t) = \int_V R(\mathbf{x}, t) P(r_s(M_w) | \mathbf{x}, t) \left| \frac{dr_s}{dM_w} \right| dV. \qquad (5)$$

The expression for $\left| \frac{dr_s}{dM_w} \right|$ is given in the Appendix. For simplicity, we assume that the probability $P(r_s | \mathbf{x}, t)$ does not depend explicitly on the absolute location $\mathbf{x}$, only on the relative location of the fault center to the injection point $|\mathbf{x} - \mathbf{x}_{inj}| = r_c$. We further assume a uniform distribution of fault centers in space. The latter is sensible in that there is no *a priori* reason that the distribution of faults should depend on injection location (although of course it could). Because, under these assumptions, the conditional distribution of events depends only on the radius of the perturbed region, equation (5) then simplifies to

$$R_t(M_w) = \left[\int_V R(\mathbf{x}, t) dV \right] P(r_s(M_w); a(t)) \left| \frac{dr_s}{dM_w} \right|$$
$$= \bar{R}(t) P(r_s(M_w); a(t)) \left| \frac{dr_s}{dM_w} \right|, \qquad (6)$$

a function parameterized by time t. Here, $\bar{R}(t)$ is the volume-integrated rate of nucleations.

To reiterate, equation (6) is correct if the probability of a particular size event is dependent only on the spatial distribution of faults, not where on the fault the nucleation occurs. Furthermore, we neglect interactions between events, such that probabilities of event sizes are not at all dependent on prior events. We proceed with these approximations, recognizing that a more complete treatment would need to account for the locations of the event hypocenters as well as fault centroids and elastic interactions between sources.

Derivation of $P(r_s; a(t))$: The 2D Case

The distribution $P(r_s; a(t))$ can be found by integrating over the conditional probability $P(r_s | \rho, r_c, r(z); a(t))$.

We first derive the 2D expression for fixed r, and later integrate over all $r(z)$. The 2D solution could also be useful if, for example, the earthquake sequence of interest occurs more or less on a single plane, such as might be observed for injection into a highly fractured zone between two more competent regions. For fixed r and time

$$P(r_s; r, \rho_{max}) = \int_0^{\rho_{max}} \int_0^{r_c^{(max)}} P(r_s | \rho, r_c; r) P(\rho, r_c; r, \rho_{max}) dr_c d\rho, \qquad (7)$$

in which ρ_{max} is the largest fault radius present, and $P(\rho, r_c; r, \rho_{max})$ is the joint distribution of fault sizes and center locations, which are sensibly taken to be independent; furthermore, the fault-size distribution is independent of $r(z)$, so $P(\rho, r_c; r, \rho_{max}) = P(\rho; \rho_{max}) P(r_c; r, \rho_{max})$.

The distribution of fault sizes is given by $P(\rho; b, \rho_{max}) = G(\rho; b)$; in which $G(\rho; b)$ is such that the resulting magnitudes are GRD-distributed with a certain b-value in the absence of stress perturbations. $G(\rho; b)$ is derived in the Appendix to be

$$G(\rho; b) = \left(\frac{2b}{\rho_m^{-2b}} \right) \rho^{-2b-1} \qquad (8)$$

(see equation A13) in which ρ_m is the smallest fault radius and b is the b-value.

Assuming that source centroids are spatially uniform implies that $P(r_c)$ linearly increases with r_c: $P(r_c) = \kappa r_c$. The constant κ is determined by the constraint that the cumulative probability over r_c is unity, but in practice can be ignored, as the final distribution can be normalized to unit area. The parameter $r_c^{(max)} = r + \rho_{max}$ is fixed by the maximum fault size, because faults located at distances greater than this do not contribute events (Fig. 2a).

There are three possible scenarios that can lead to earthquakes with radius r_s. The first is shown in Figure 2b (case 1). The probability that an earthquake occurring on a fault with radius ρ will be completely inside the perturbed region (shown as the large circle with solid outline) is given by the ratio of areas A/B, and denoted P_{in} by Segall and Lu (2015). Area A is where the faults are fully contained within the region; B is where the same size faults have at least one point

within the perturbed region. The condition that the fault be completely within the perturbed zone is $r_c \leq r - \rho$.

The second case is shown in Figure 2c (case 2) and represents sources only partially within the perturbed region such that the earthquake sizes are $r_s < \rho$. The probability of these partial events is denoted by P_p. For simplicity, we consider the earthquake radius to be the largest inscribed circle between the fault and the perturbed region. Case 2 occurs for sources with centers r_c located within the range $r - \rho \leq r_c \leq r + \rho$. The radius r_s of a partial event is a function of r_s, r_c, and ρ: $r_s = (\rho + r - r_c)/(2)$, as discussed in detail below and shown in Figure 3.

Case 3 is the special case when a fault with radius $\rho > r$ completely covers the perturbed area. Under our stated assumptions, the resulting earthquake will have radius equal to r because the background stress outside the region is too low to allow the earthquake to continue to propagate, even though the fault extends beyond this region. The probability of an earthquake with radius $r_s = r$, denoted by P_r, occurring on a fault large enough to cover the entire region is given by the ratio of areas C/D (Fig. 2d). Area D is the circle such that any fault with radius ρ and centroid $r_c \leq \rho + r$ touches the perturbed zone with at least one point, whereas area C is the circle such that any fault with radius ρ and centroid $r_c \leq r + (\rho - 2r) = \rho - r$ completely covers the perturbed region.

Thus, the total description of event radius r_s can be determined geometrically as a piecewise function of ρ, r_c, and, r as shown in Figure 3. Mathematically:

$$r_s = \begin{cases} \rho & \text{if } \rho < r \text{ and } r_c < r - \rho \\ \frac{\rho + r - r_c}{2} & \text{if } |r - \rho| < r_c < r + \rho \\ r & \text{if } \rho > r \text{ and } r_c < \rho - r \\ 0 & \text{if } r_c > r + \rho \end{cases} \quad (9)$$

Figure 3a composes two plots superimposed, with the lower and left axes together and the upper and right axes together. Source centroid location r_c is plotted on both horizontal axes, and r_s is plotted on both vertical axes, but the scales are different based on whether ρ (fault radius) is greater than or less than r. For $\rho < r$, use the left and lower sides of the graph, and for $\rho > r$, read the upper and right sides. The second expression in equation (9) above can be derived by considering Figure 3b. This applies to faults located partially
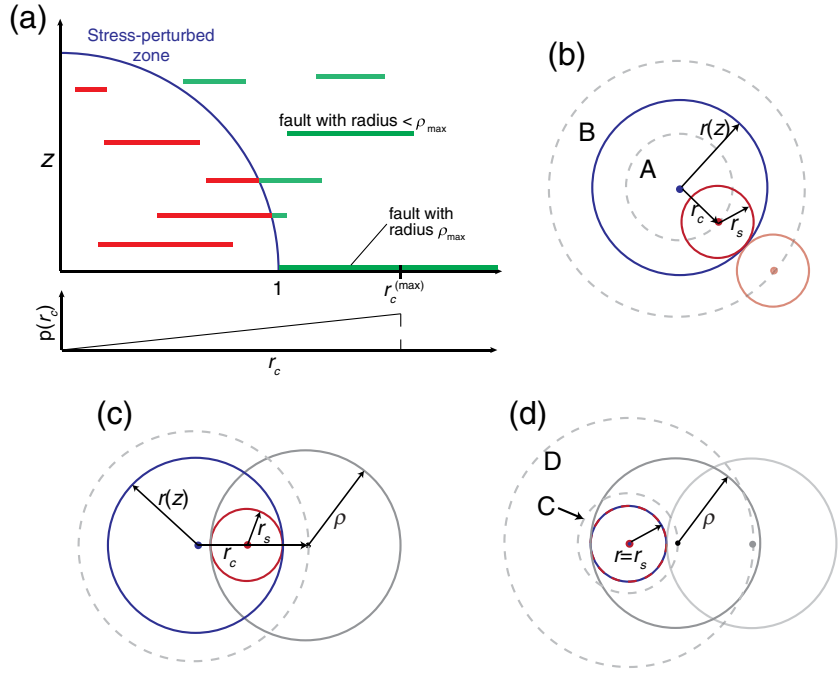
Figure 2. Diagrams illustrating the distribution of r_c and how faults contribute event sizes depending on their relative location to the perturbed region. (a) Upper: schematic showing a cutaway view of one quadrant of the stress-perturbed region, with example fault locations shown. Only faults or parts of faults inside the perturbed region host earthquakes. Length scales in this diagram are normalized by $a(t)$ such that $r_c^{(\text{max})} = 1 + (\rho_{\text{max}}/a(t))$. Lower: probability distribution of r_c. x axis in both diagrams is r_c. (b–d) Cases that produce r_s-size earthquakes. Circles with radius r or $r(z)$ denote slices through the stress-perturbed region. Circles with radius ρ represent faults; circles with radius r_s represent earthquakes. (b) Case 1 (P_{in}): a fault with radius ρ is completely inside the perturbed region and produces an earthquake with radius $r_s = \rho$. Dashed circles outline areas A and B with radius $r - r_s$ and $r + r_s$, respectively. (c) Case 2 (P_p): a fault that is partially inside the perturbed region and produces an earthquake with radius $r_s < \rho$. The fault may lie on any point of the dashed circle and contribute an r_s-size event. (d) Case 3 (P_r): a fault with radius ρ completely covering the perturbed region such that the earthquake has radius $r_s = r(z)$. A second fault of the same size is shown that just touches the edge of the perturbed region, and its center outlines the outer dashed circle. Areas C and D are denoted by the dashed circles and have radius $\rho - r$ and $\rho + r$, respectively. The color version of this figure is available only in the electronic edition.

inside the perturbed region (corresponding to case 2 in Fig. 2c).

The probability $P(r_s | \rho, r_c, r)$ is uniquely determined from equation (9)

$$P(r_s | \rho, r_c; r) = \begin{cases} \delta(\rho - r_s) & \text{if } \rho < r \text{ and } r_c < r - \rho \\ \delta\left(\frac{\rho + r - r_c}{2} - r_s\right) & \text{if } |r - \rho| < r_c < r + \rho \\ \delta(r - r_s) & \text{if } \rho > r \text{ and } r_c < \rho - r \\ 0 & \text{if } r_c > r + \rho \end{cases} , \quad (10)$$

in which δ is the Dirac delta function.

To find $P(r_s; r)$, substitute equation (10) into equation (7) by decomposing the integral into the sum of four terms, one each for the first and third lines in equation (10), and two for the second (accounting for faults larger or
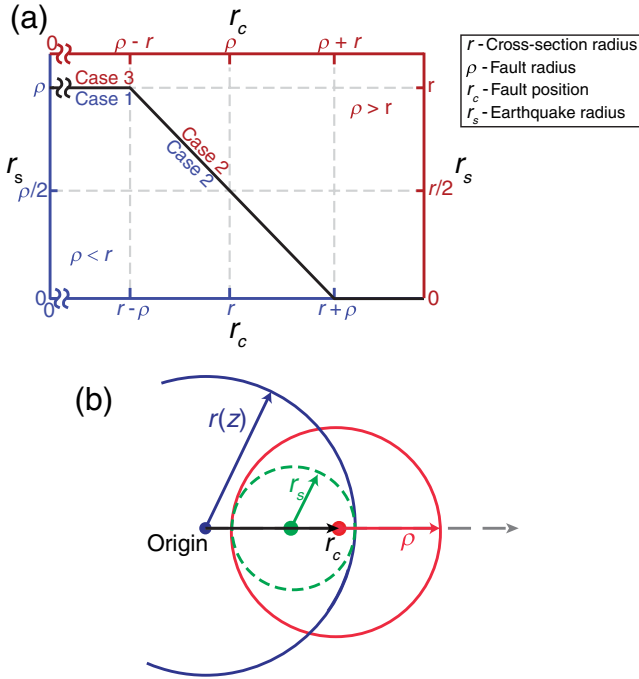
Figure 3. (a) Graph of the function that maps r, ρ, and r_c to the rupture radius r_s under the assumptions employed here. The left and lower axes are for $\rho < r(z)$ and the right and upper axes are for $\rho > r(z)$. Both horizontal axes are r_c and both vertical axes are r_s, but the scales are different. (b) Details of the geometry for computing r_s for partial sources. The origin is the center of the perturbed region with radius $r(z)$ (r in the 2D case), and the fault with radius ρ has centroid located at r_c. The earthquake size is taken to be the largest inscribed circle between the fault and the perturbed region: $2r_s = r(z) - (r_c - \rho)$. The color version of this figure is available only in the electronic edition.

smaller than r separately). This gives the following expression for $P(r_s)$:

$$
\begin{aligned}
P(r_s;r)/\kappa = & \int_0^{\rho_{max}} \left[\int_0^{r-\rho} r_c dr_c \right] \delta(\rho - r_s) G(\rho;b) d\rho \\
& + \int_0^r \left[\int_{r-\rho}^{r+\rho} \delta\left(\frac{r+\rho-r_c}{2} - r_s \right) r_c dr_c \right] G(\rho;b) d\rho \\
& + \int_r^{\rho_{max}} \left[\int_{\rho-r}^{\rho+r} \delta\left(\frac{r+\rho-r_c}{2} - r_s \right) r_c dr_c \right] G(\rho;b) d\rho \\
& + \delta(r - r_s) \int_r^{\rho_{max}} \left[\int_0^{\rho-r} r_c dr_c \right] G(\rho;b) d\rho.
\end{aligned}
$$
(11)

The first term corresponds to case 1 in Figure 2b and the first line of equation (9), which we label P_{in}^{2D} for faults fully inside the perturbed region. The second and third terms both correspond to case 2; the second is for $\rho < r$ and the third is for $\rho > r$; these terms together are labeled P_p^{2D}, for partial sources. The fourth term corresponds to case 3 and the third line of equation (9), which we label P_r^{2D} for earthquakes with size equal to $r(z)$.

To evaluate equation (11), we take each term in turn. Integrating the first term over r_c, then over ρ leads to:

$$
P_{in}^{2D}(r_s;r) = \int_0^{\rho_{max}} \delta(\rho - r_s) \frac{(r-\rho)^2}{2} G(\rho;b) d\rho = \frac{(r-r_s)^2}{2} G(r_s).
$$
(12)

The second and third terms are the partial sources P_p. We can integrate over the delta distributions by rearranging their arguments using standard identities, paying careful attention to the corresponding limits in the integral over ρ. For the second term in equation (11), this gives

$$
\begin{aligned}
P_{p1}(r_s;r) = & \int_0^r \int_{r-\rho}^{r+\rho} 2\delta(r_c - (r+\rho - 2r_s)) r_c dr_c G(\rho;b) d\rho \\
= & 2 \int_{r_s}^r (r+\rho - 2r_s) G(\rho;b) d\rho.
\end{aligned}
$$
(13)

The lower integration limit on ρ follows from the fact that the fault radius cannot be smaller than that of the resulting earthquake r_s.

The third term in equation (11), which is the second term for partial sources, is given by:

$$
\begin{aligned}
P_{p2}(r_s;r) = & \int_r^{\rho_{max}} \int_{\rho-r}^{\rho+r} 2\delta(r_c - (r+\rho - 2r_s)) r_c dr_c G(\rho;b) d\rho \\
= & 2 \int_r^{\rho_{max}} (r+\rho - 2r_s) G(\rho;b) d\rho.
\end{aligned}
$$
(14)

The two integrals for partial sources (equations 13 and 14) can be combined into a single expression:

$$
P_p^{2D}(r_s;r) = 2 \int_{r_s}^{\rho_{max}} (r + \rho - 2r_s) G(\rho;b) d\rho.
$$
(15)

The fourth and final term gives the probability of earthquakes of size r

$$
P_r^{2D}(r_s;r) = \frac{1}{2} \delta(r_s - r) \int_r^{\rho_{max}} (\rho - r)^2 G(\rho;b) d\rho,
$$
(16)

which is only nonzero at exactly $r_s = r$. The delta function nature of this term comes from the unrealistic assumption of a hard boundary on rupture extent, equal to the dimension of the source region. All sufficiently large sources that enclose this area produce exactly the same size event. A more realistic model might account for a range of event sizes in this scenario that would be determined probabilistically in some way. Such an approach would essentially smear out the delta function at $r_s = r$.

The total probability $P(r_s)$ for fixed $r(z)$ is given by adding the various contributions

$$
P^{2D}(r_s;r) = \kappa[P_{in}^{2D}(r_s) + P_p^{2D}(r_s) + P_r^{2D}(r_s = r)],
$$
(17)

in which the individual terms are given by equations (12), (15), and (16).
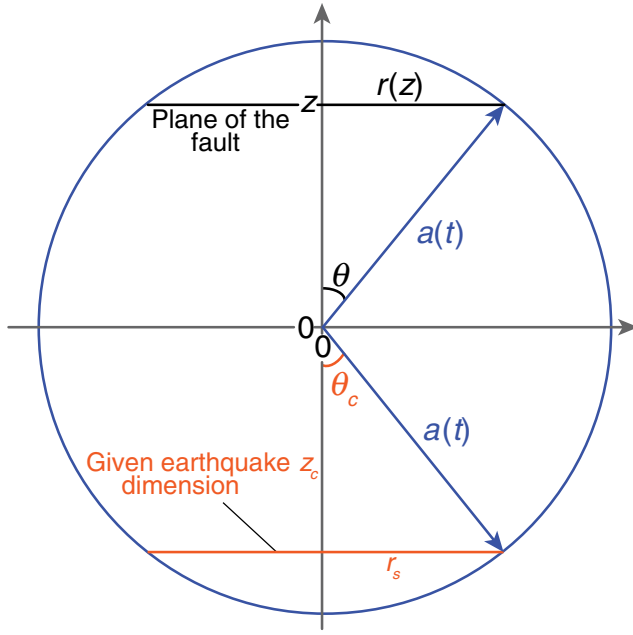
Figure 4.   Figure showing how to compute $r(z)$ for a given z and z_c for a given r_s. The diagram shows the perturbed region perpendicular to the z direction. The upper part of the graph shows that $r(z) = \sqrt{a(t)^2 - z^2}$. The lower part shows that the maximum value of z at which earthquakes of radius r_s just fit inside the perturbed region is given by $z_c = \sqrt{a(t)^2 - r_s^2}$. The color version of this figure is available only in the electronic edition.

The integration over the distribution of fault radii ρ may need to be done numerically for general forms of $G(\rho; b)$. In the Appendix, we derive the exact form of $G(\rho; b)$ assuming the GRD and incorporate this form directly into the solution for $P(r_s)$.

Derivation of $P(r_s; a(t))$: The 3D Case

To determine $P(r_s)$ for the 3D case, treat z as a random variable and integrate the 2D distribution from equation (17) over z

$$P(r_s; a) = \int_{-a}^{a} P^{2D}(r_s | r(z); a, \rho_{max}) p(z) dz, \quad (18)$$

in which $P^{2D}(r_s | r(z); a, \rho_{max})$ is given by equation (17). From Figure 4, the cross-sectional radius of a 2D slice through the sphere at z is given by $r(z) = \sqrt{(a^2 - z^2)}$, in which a is the radius of the perturbed region. $P(z)$ is uniform on the interval $[-a, a]$ with probability density $P(z) = 1/2a$. The integrand is symmetric in z, so equation (18) reduces to

$$P(r_s; a, \rho_{max}) = \frac{1}{a} \int_{0}^{a} P^{2D}(r_s | r(z); a, \rho_{max}) dz. \quad (19)$$

The final consideration is the bounds on z for each term in equation (17). These can be obtained by noting from Figure 4 that the largest earthquake obtainable at a given z has radius $r_s = \sqrt{a^2 - z^2}$. For a given r_s, the maximum pos-

sible $|z|$ that contains this source is thus $z_c = \sqrt{a^2 - r_s^2}$, as shown in Figure 4.

Sources Fully inside (P_{in}).   The first term in equation (17) is found by setting $r(z) = \sqrt{a^2 - z^2}$ and integrating over the range $0 < z < z_c$

$$P_{in}(r_s) = \frac{G(r_s)}{2} \int_{0}^{z_c} \left(\sqrt{(a^2 - z^2)} - r_s \right)^2 dz$$

$$= \frac{G(r_s)}{2} \left[a^2 z_c - a^2 r_s \cos^{-1}\left(\frac{r_s}{a}\right) - \frac{z_c^3}{3} \right] \quad (20)$$

(see Fig. 4) consistent with the results of Segall and Lu (2015). Normalizing $z_c' = \sqrt{1 - r_s'^2}$, in which $ar_s' = r_s$ and $az_c' = z_c$, shows that the scaling of the sphere can be neglected in the derivation. Thus, for the rest of the derivations, we scale all lengths by $1/a(t)$ to work with a unit sphere, and we drop the prime notation for conciseness unless needed for clarity.

Partial Sources.   Integrating $P_p^{2D}(r_s | r(z))$ over z

$$P_p(r_s) = 2 \int_{r_s}^{\rho_{max}} \left[\int_{0}^{z_c} \left(\sqrt{1 - z^2} + \rho - 2r_s \right) dz \right] G(\rho; b) d\rho$$

$$= \int_{r_s}^{\rho_{max}} [\cos^{-1}(r_s) + (2\rho - 3r_s)z_c] G(\rho; b) d\rho, \quad (21)$$

in which we reversed the order of integration, noting the limits are constants with respect to ρ and z.

Earthquake Sizes Equal to r.   We show in the Appendix that integrating the third term for P_r gives

$$P_r(r_s) = \frac{1}{2} \frac{r_s}{z_c} \int_{r_s}^{\rho_{max}} (\rho - r_s)^2 G(\rho; b) d\rho. \quad (22)$$

Final Result.   From equation (6), the total probability of events in time and magnitude is

$$R(M_w, t) = \bar{R}(t) P(r_s(M_w) | r_c; a(t), \rho_{max}) \left| \frac{dr_s}{dM_w} \right|, \quad (23)$$

in which $\bar{R}(t)$ is the volume-integrated rate of earthquake nucleations.

The probability $P(r_s' = r_s/a(t))$ can be written as the sum of the three terms previously labeled as the sources fully inside, partially inside, and fully overlapping the perturbed region:

$$P(r_s'; \rho_{max}) = \kappa[P_{in}(r_s') + P_p(r_s'; \rho_{max}) + P_r(r_s'; \rho_{max})]. \quad (24)$$

Substituting equations (20)–(22) into equation (24) gives

$$P(r_s'; \rho_{\max}) = \frac{\kappa}{2}\left[z_c - r_s' \cos^{-1}(r_s') - \frac{z_c^3}{3}\right]G(r_s)$$

$$+ \kappa \int_{r_s'}^{\rho_{\max}}[\cos^{-1}(r_s') + (2\rho - 3r_s')z_c]G(\rho; b)d\rho$$

$$+ \frac{\kappa r_s'}{2 z_c}\int_{r_s'}^{\rho_{\max}}(\rho - r_s')^2 G(\rho; b)d\rho. \qquad (25)$$

The probabilities depend on the fault-size distribution $G(\rho; b)$. Integrating over ρ (as we do in the Appendix using the GRD) gives the final distribution for fault radii. These expressions are given in equations (A23) and (A27); because the expressions are lengthy we do not repeat them here. We also show in the Appendix that if $b > 1$, it is possible to allow $\rho_{\max} \to \infty$, whereas for $b \le 1$, $\rho_{\max}$ must be specified for the distribution to converge.

To transform the posterior probability distribution $P(r_s)$ to $P(M_w)$, use

$$\left|\frac{dr_s}{dM_w}\right| = \left[\frac{\ln(10)}{2((\pi/c)\Delta\tau)^{1/3}}10^{(M_w+6.03)/2}\right] \qquad (26)$$

(derived in the Appendix), in which $\Delta\tau$ is the stress drop, and $c = 7\pi/16$ is a geometrical constant. Combining this with equation (25) into equation (23) gives the final distribution of earthquake magnitudes for a given time.

Equation (25) is for a fixed radius, $a(t)$ and hence time. To obtain the time-integrated distribution, it is necessary to numerically integrate equation (23) with equation (26) to get the final distribution on event magnitudes for all time.

Discussion

Example Simulations

The results presented in the Method section provide the complete time-dependent FMDs for seismicity restricted by the perturbed volume, as well as allow for fast simulations of earthquake magnitudes. Inputs to the model are the time-dependent radius of the perturbed region $a(t)$ and the volume-average rate of nucleations $\bar{R}(t)$. Parameters are the b-value, the largest fault radius, and the stress drop. We assume constant stress drop to compute magnitude with the scaling $\Delta\tau \sim \mu(\Delta u/r_s)$, in which Δu is average slip and μ is shear modulus. Results of the current study provide the FMD that varies in time, which can be sampled to provide simulated seismicity catalogs. Figure 5 shows the relative contributions from P_{in}, P_p, and P_r for various parameter values, at snapshots in time (fixed $a(t)$). Plots (a) and (b) assume a maximum fault size of 0.5 km, whereas plots (c) and (d) assume $\rho_{\max}$ of 1.5 km; $a = 0.25$ km for plots (a) and (c) and 2.5 km for plots (b) and (d).

Because we have assumed $r(z)$ is the upper bound on rupture size, and the dominant contribution to this term is from faults with radii larger than a (when they exist), when $a \gg \rho_{\max}$, P_r does not contribute events (Fig. 5b,d).

Figure 6 shows FMDs at snapshots in time comparing the predicted FMD from the current model to that of Segall and Lu (2015), as well as the GRD for the same parameter values as Figure 5. Lines are the theoretical results; symbols show numerically simulated results for both the current model and the Segall–Lu result. The numerical simulation is conducted by randomly drawing from the distributions on z, fault centroid locations r_c, and fault radii ρ, and computing the resulting r_s using equation (9). Vertical dashed lines show the magnitude corresponding to $a(t)$, and the maximum magnitude (corresponding to $\rho_{\max}$) is shown if less than $a(t)$.

As expected, the distribution changes significantly for different $\rho_{\max}/a$. In all cases, the model presented here predicts more events at each magnitude than the Segall–Lu model, as is expected because we include the additional terms P_p and P_r. For large values of $\rho_{\max}/a$, the FMD for the current study predicts a significantly higher rate of events than the Segall–Lu model, whereas for small $\rho_{\max}/a$ the two models are similar, because P_{in} dominates the other two terms.

The increase in the frequency of events relative to the GRD seen in Figure 6a,c is due to the P_r term. Those result from the hard boundary on event size at $a(t)$; sources that completely cover the perturbed region contribute an $r(z)$-radius event. The increase is significantly less than that predicted by the upper end-member model of Shapiro et al. (Shapiro et al., 2011, 2013; Shapiro, 2015) because they assumed the entire fault would rupture once nucleated. In the model, we explore here, both nucleations and ruptures are limited by V.

We construct theoretical FMDs assuming 150 days of constant injection rate and a diffusivity of $D = 0.01$ m^2/s (Fig. 7). The instantaneous FMDs are shown every four days, shaded by the time since the onset of injection, for P_{in} only (Fig. 7a), $P_{in} + P_p$ (Fig. 7b), and the full model including P_r (Fig. 7c). Ordinary GRD is the dashed line in each plot. The insets show the time-integrated FMD that would be observed integrating over all 150 days of injection assuming a constant rate of seismicity. When only P_{in} is included, significant roll-off occurs, especially at short times, and the time-integrated FMD falls off faster. With $P_{in} + P_p$, the FMDs follow GRD except at the high magnitudes, in which rolloff occurs, and cuts off at $a(t)$. With all terms included, the FMDs uptick at $a(t)$ (Fig. 7c). In this case, rolloff eventually occurs at late times when $\rho_{\max}/a(t)$ is small and the largest fault size becomes the limiting dimension for events. The inset in Figure 7c shows all three time-integrated plots for comparison. In this case, the time-integrated distribution is dominated by P_{in} and P_p.

In Figure 7, the instantaneous magnitude distributions transition from having a sharp uptick at $a(t)$ to rolling over as $a(t)$ approaches $\rho_{\max}$. We consider it very unlikely that the sharp uptick would be observed in reality, because the hard boundary on rupture size such as we have imposed is not likely to occur in nature. Rather, events may arrest over some range of distances. In the low stress limit we envision, this range could be small, so we approximate it as a hard boundary. Also note that the distribution of events integrated over
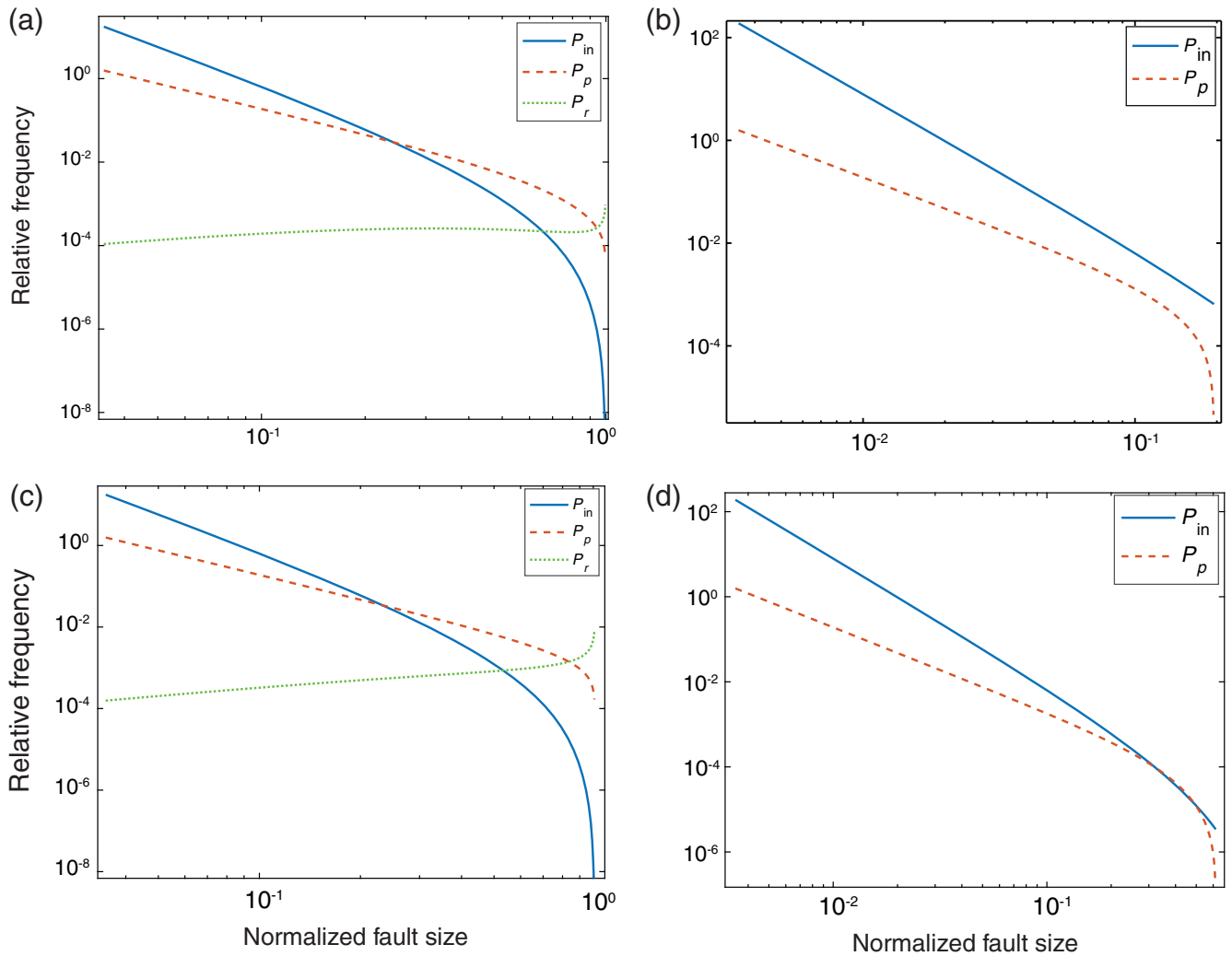
Figure 5. Relative contributions of each term in equation (25) for a *b*-value of 1. *x* axis shows fault radius normalized by *a*, and *y* axis shows the relative frequency of event sizes. (a,b) $\rho_{max} = 0.5$ km, equivalent to $M_w = 4$; (a) $a(t) = 0.25$ km, $\rho_{max}/a = 2$; (b) $a(t) = 2.5$ km, $\rho_{max}/a = 0.2$. (c,d) $\rho_{max} = 1.5$ km ($M_w = 5$); (c) $a(t) = 0.25$ km, $\rho_{max}/a = 6$; (d) $a(t) = 2.5$ km, $\rho_{max}/a = 0.6$. The color version of this figure is available only in the electronic edition.

time smoothes out these upticks as $a(t)$ grows. Both of these effects result in a bump in the distributions instead of a sharp peak (e.g., see Figs. 8–10).

Comparison to Gutenberg–Richter

In this study, we derived expressions for the instantaneous FMDs for faults that follow the GRD, with the constraint that earthquakes only occur within a stress-perturbed region. One can integrate the instantaneous FMDs over time to see how, given a seismicity rate history, the time-integrated FMD compares to the GRD. This involves weighting the instantaneous FMDs at each timestep by the rate of seismicity at that time (equation 23). The time-integrated FMD for any sequence thus depends on both the size of the perturbed region and the rate of events, as well as the *b*-value, maximum fault size, and assumed stress drop. Sample time-integrated FMDs are shown in Figure 8 for a constant seismicity rate. For

$b = 1$, the distribution predicts more large events than ordinary GRD for some range of magnitudes, prior to the distribution rolling over at the magnitude corresponding to the (time-dependent) perturbed zone radius $a(t)$. To reiterate, this is due to the restriction on event sizes to be equal to or less than the size of the perturbed region. Larger sources can only contribute events with radius as large as $a(t)$, so the larger sources fold over into smaller events. For $b = 1.4$, there are fewer events predicted than the GRD. ρ_{max} in these simulations is approximately 1550 m, corresponding to $M_w^{(max)} = 5$.

In the model presented here, the distribution of event sizes depends on both the geometrical terms and the total rate of events. From the inset in Figure 8, it can be seen that the time-integrated FMDs can be very similar to ordinary Gutenberg–Richter (GR). We discuss this issue further in reference to an example simulation as well as two actual induced sequences.
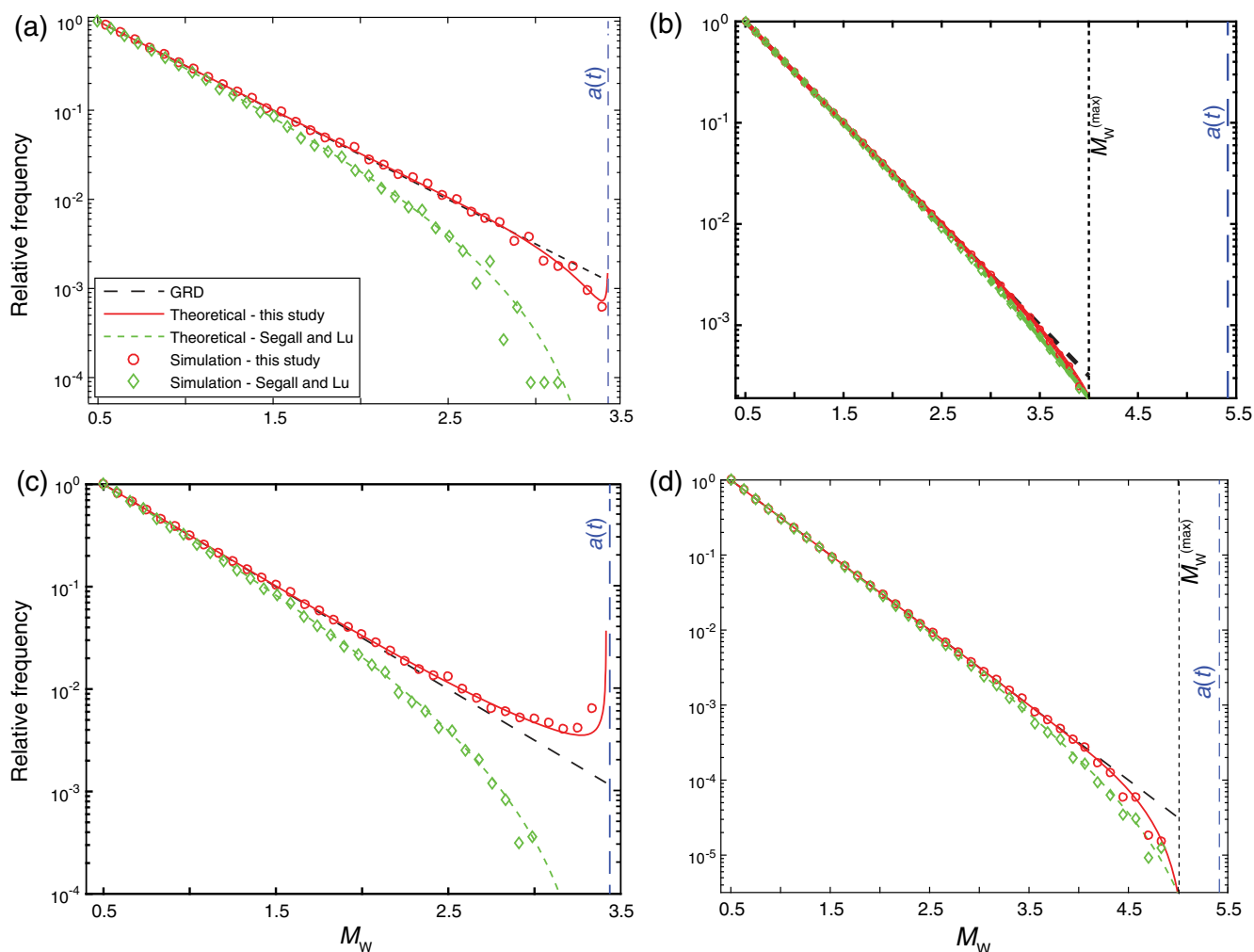
Figure 6. Comparison of the current study with the Segall and Lu (2015) model and ordinary Gutenberg–Richter (GR), including both theoretical and example simulation results. Values of ρ_{max} and $a(t)$ correspond to those in Figure 5. The color version of this figure is available only in the electronic edition.

Comparison to Previous Work

Figure 9 compares the result from the current study with Segall and Lu (2015) and Shapiro *et al.* (Shapiro *et al.*, 2011, 2013; Shapiro, 2015). Figure 9a shows the time-integrated FMDs for each model, normalized to the same number of events, integrating up to $a(t) = 100$ m. For these simulations, $b = 1$, $M_c = 0$, and $M_{max} = 5$. The Segall and Lu (2015) model (referred to as P_{in} in this study) is identical to the lower end-member model of Shapiro *et al.* The model presented in this study truncates at a magnitude corresponding to $a(t) = 100$ m, or M_w 2.53, as does the lower Shapiro *et al.* model. The upper end-member model truncates at $M_{max} = 5$. Figure 9b shows the ratio of each model to ordinary GRD as a function of magnitude. The difference between the present model and the upper- and lower-bound models is a direct consequence of the assumptions we made about the stress conditions of the system: nucleations may occur on any fault inside the perturbed region, but the size of events are limited by the low background stress to only rupture the fraction of the fault inside the perturbed region.

Both the FMD derived in the present study and the Shapiro *et al.* upper end-member FMD predict more events than GRD for a range of magnitudes. In the Shapiro *et al.* model, this is because any fault with at least a small fraction inside the perturbed volume V experiences a full rupture. In contrast, the FMD derived in this study allows for nucleation on faults that overlap V, but events may only be as large as the part of the fault contained within V. This assumption of a hard boundary on ruptures at $a(t)$ results in the slight increase in probability just below the corresponding magnitude, because larger faults that intersect the region contribute events only as large as $a(t)$. In our model, no events larger than $a(t)$ occur, but in the Shapiro upper end-member model, earthquakes of arbitrarily large size may occur due to stimulation, a limit we associate with a high background shear to normal stress ratio.

Earthquakes post Shut-in

A significant concern for hazard management is that the largest induced earthquake can occur after the injection well
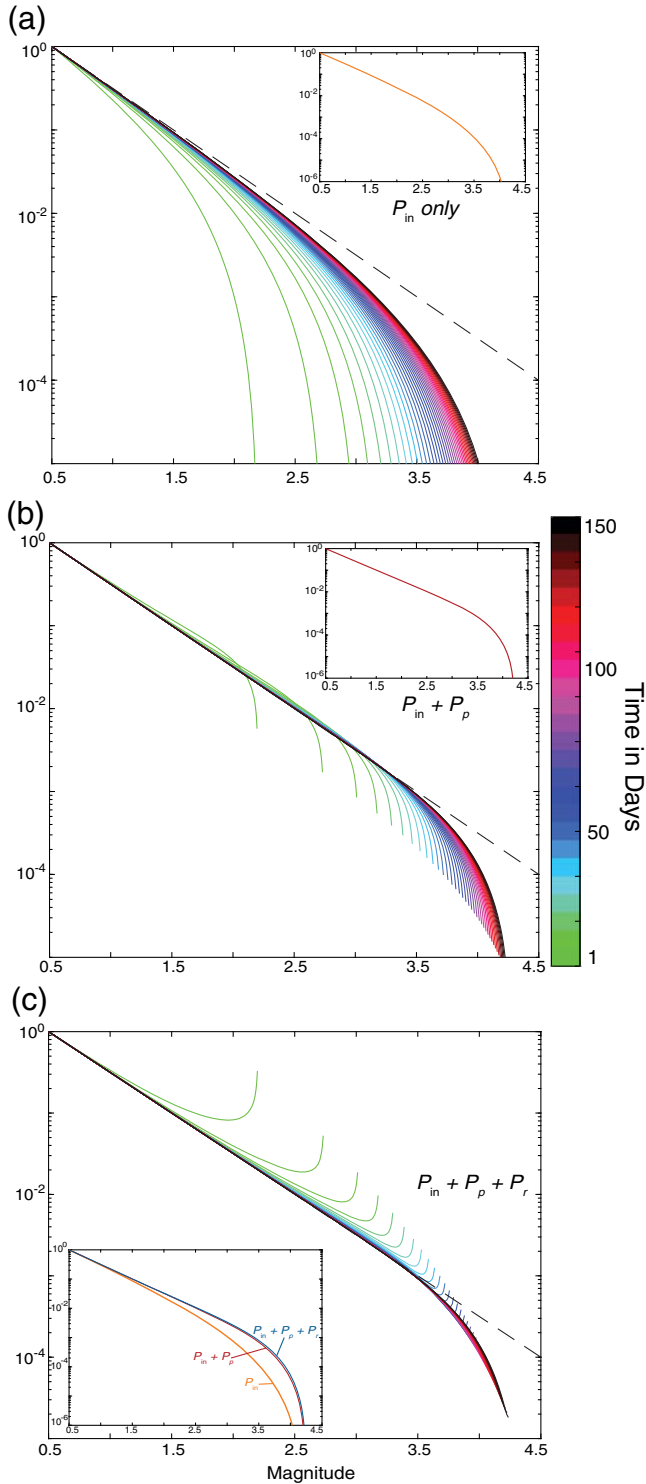
Figure 7. Instantaneous frequency–magnitude distributions (FMDs) every 4 days for 150 days of simulated injection, assuming a diffusivity of 0.01 m²/s. Insets show the time-integrated (overall) FMD obtained by integrating over 150 days assuming a constant rate of seismicity. $M_w^{(\max)} = 4.5$ and $b = 1$. The dashed line shows the Gutenberg–Richter distribution (GRD). (a) P_{in} only, as in Segall and Lu (2015); (b) $P_{in} + P_p$; (c) $P_{in} + P_p + P_r$. This is the complete solution for $P(r_s)$ from equation (25). The inset in (c) shows all three time-integrated plots. The color version of this figure is available only in the electronic edition.

has been shut in (e.g., Deichmann and Giardini, 2009; Dorbath *et al.*, 2009; Kim, 2013). One possible mechanism for this is that pore-pressure diffusion continues away from the injector after shut-in, and as a result, the size of the stress-perturbed region continues to grow for some time.

To explore this, we simulate a sequence of events using the rate of earthquakes from Segall and Lu (2015, fig. 17), scaled to give a total of 10,000 events (Fig. 10). Injection occurs at a constant rate from day 1 to day 15, then ceases. The radius of the perturbed region (black line in Fig. 10a) grows proportionally to $\sqrt{ct}$, with $c = 0.0679$ m²/s. Samples are drawn randomly from both the GRD and equations (A27) and (23), using a *b*-value of 1 and $M_w^{\max} = 6$($\rho_{\max} \approx 4.9$ km).

Figure 10 shows several noteworthy features:

1. The largest event in this simulation occurs just after shut-in. This happens because at early times after shut-in, pore-pressure diffusion continues away from the injector, and the total rate of events is still high (and actually increases very slightly due to poroelastic effects; for explanation, see Segall and Lu, 2015). There is statistical variability in this result; some simulations using the same parameters did not show the largest event occurring after shut-in.

2. During the injection phase, more events are expected at magnitudes just below the rolloff magnitude than ordinary GR (Fig. 10b; the rolloff here is not at $M_w^{\max}$, but at $a(t)$). After injection ceases diffusive spreading continues but the rate of events decreases. If the plots were extended to much lower rates and higher magnitudes, the same increase in rate, as seen during the injection phase, would be seen in the postinjection phase.

3. The largest magnitude events during the post-shut-in phase appear to be much greater than that predicted by the theoretical FMD. This is because the FMD is time integrated; at early times, the theoretical FMD is much more similar to the injection-phase FMD, but the contribution to the overall postinjection phase is small. It is precisely this point at which the model predicts the largest magnitude event could be observed, when the rate of events is still high and the perturbed region is still growing in time, as is observed in this simulation.

4. Ordinary GR predicts larger events at short times than the present study, as seen in Figure 10a, in which some events exceed the magnitude cutoff at short times. Some of the events generated using the approach described in this study can also be seen to lie directly on the line, indicating that a slightly larger event would likely have occurred in the absence of a hard bound on event size.

We note that limiting the largest magnitude in the low-stress environment can actually slightly increase the number of events at magnitudes just below the rolloff (Fig. 10b), relative to simply truncating ordinary GRD. The effect will in general depend on the specific parameters (*b*-value, $\rho_{\max}$) seismicity rate $\bar{R}(t)$, and the perturbed region expansion $a(t)$. For some parameters, there is no increase relative to the
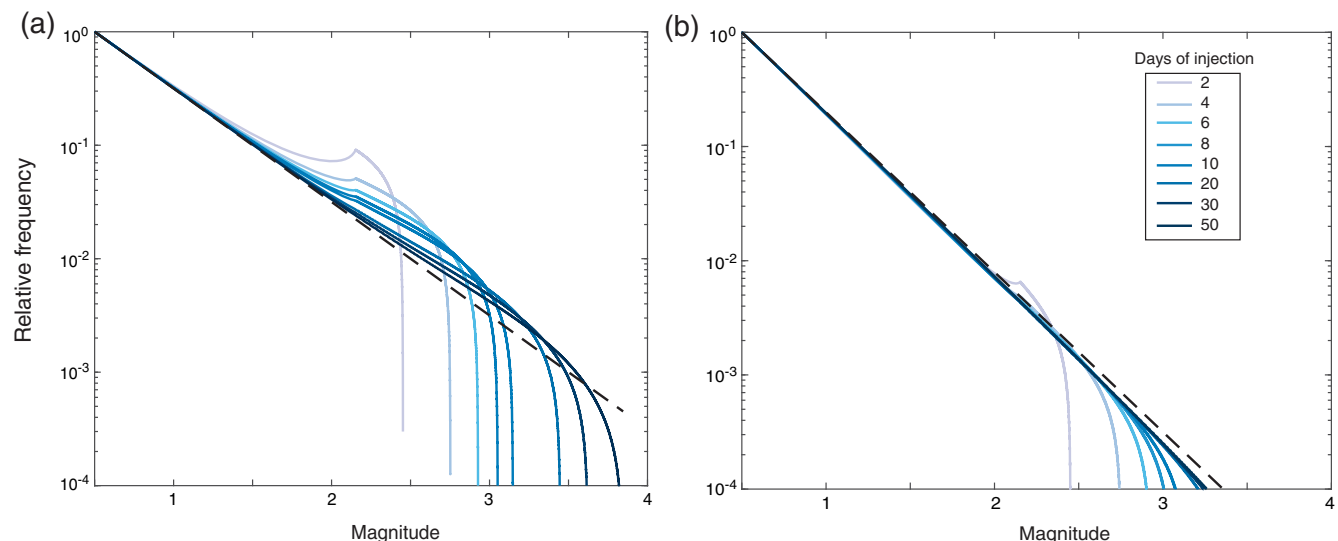
Figure 8. Comparison of this study with ordinary (nontruncated) GR over several days of injection, assuming a constant rate of events. Parameters are $c = 0.01$ m^2/s, $M_w^{(max)} = 5$, and $M_c = 0.5$. Curves show the time-integrated FMD from this study for 2, 4, 6, 8, 10, 20, 30, and 50 days. The perturbed radius is assumed $2\sqrt{ct}$. (a) b-value $= 1$; (b) b-value $= 1.4$. The color version of this figure is available only in the electronic edition.
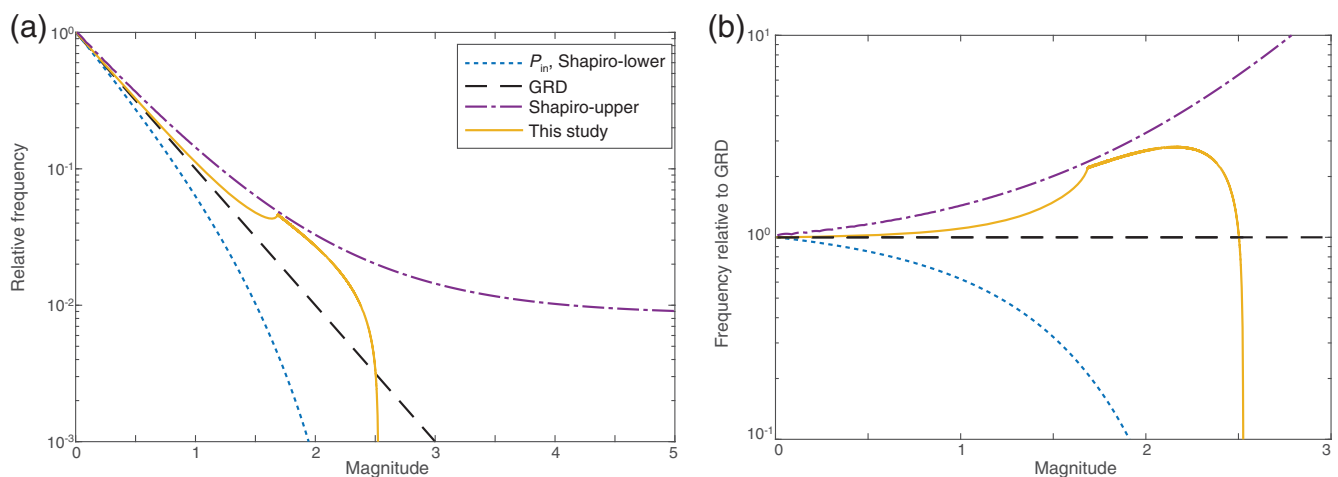

Figure 9. Comparing the models of Segall and Lu (2015) and Shapiro *et al.* to this study. These plots use $b = 1$, $M_c = 0$, and $M_{max} = 5$, and we integrate in time from the initial start of injection until $a(t) = 100$ m. (a) Frequency versus magnitude plot, normalized to have the same total rate of events. The model presented by Segall and Lu (2015) (P_{in} in this study) is identical to the lower end-member model of Shapiro *et al.* The upper end-member model truncates at $M_w = 5$, the maximum fault size in this simulation. (b) Ratio of each model to ordinary GRD. The color version of this figure is available only in the electronic edition.

truncated GRD (Fig. 8b). We ignore the propagation of decreasing pore pressure away from the injector after shut-in. If earthquakes cannot rupture through a region of low pore pressure, this would impact the distribution of event sizes. We also ignore interactions between sources, which could also impact the magnitude distribution.

As can be seen from the time-integrated distributions in Figure 10b, the FMD at lower magnitudes (or late times) is similar to the GRD, so distinguishing between these two models without a very complete earthquake catalog could be difficult. To illustrate this problem, we show data from two induced seismicity sequences in Figure 11: the Basel

Enhanced Geothermal System (EGS) sequence (Kraft and Deichmann, 2014), and the Paralana (Cooper basin, Australia) EGS sequence from 2009 (Albaric *et al.*, 2014). For both of these sites, we fit a diffusion curve to the cloud of seismicity as an approximation for the size of the perturbed volume V, and then compare the corresponding magnitude of an event fully spanning the region to the observed seismicity. (Estimating M_{max} using the relation of McGarr and Barbour, 2017, instead of the seismicity cloud gives similar results for stress drops of 1–3 MPa, typical for the Basel earthquakes; Goertz-Allmann *et al.*, 2011.) In both cases, it can clearly be seen that the observed magnitudes do not come close to this
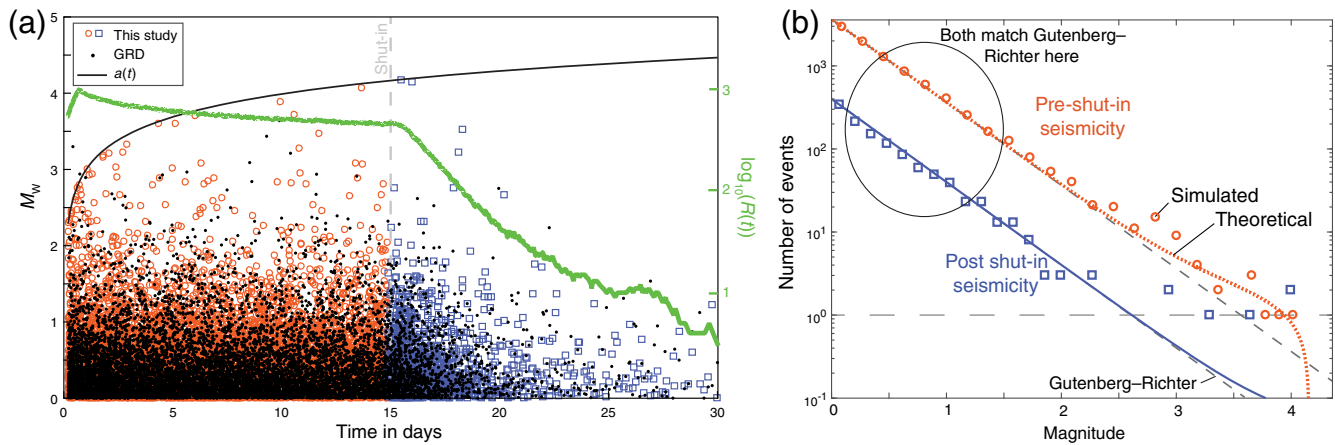
Figure 10. Example simulation of GRD and FMD from this study. (a) Magnitudes over time. The vertical dashed line shows the shut-in time, and the thin solid line shows the radius of perturbed zone (in magnitude units). The thicker line and corresponding axis shows log (total rate of events), from Segall and Lu (2015, fig. 17) scaled to produce a total of 10,000 events. (b) Observed FMD for pre- and post-shut-in events from (a), as well as the theoretical distributions from this study, with the GRD for comparison. The dashed horizontal line is the one-event threshold. The color version of this figure is available only in the electronic edition.

limit, even at very early times. However, fitting a diffusion curve to the seismicity, though widely practiced, ignores the impact of static and especially dynamic stress transfer between events, which could significantly overestimate the volume stimulated by pore-pressure diffusion.

Recall that we assumed (as do Segall and Lu, 2015; Shapiro, 2015) that the background distribution of event sizes follows GR. Figure 11 may be compared with the simulation in Figure 10, which has a very high rate of events initially and thus several events that are limited by the size of V. The Basel and Paralana sequences may not generate enough earthquakes to sample the limits of V. We conclude that either V is overestimated by fitting a diffusion profile, or there are not enough large events in either of these sequences to test whether or not events are bounded by the perturbed volume. The predictions of the model presented in this study are nearly identical to GR in the observed range of magnitudes for both of these injection sequences.

van der Elst *et al.* (2016) also argue that most induced sequences do not contain enough events to generate magnitudes close to the volume-based limit suggested by McGarr (2014). The induced seismicity sequences that do contain enough events to potentially test the hypothesis are the recent large earthquakes in Oklahoma at Prague, Fairview, Cushing, and Pawnee. These may provide evidence that events are limited by injected volume (McGarr and Barbour, 2017), but are more difficult to interpret in the context of a single point injector in a homogeneous medium.

General Tests for Time-Varying FMDs

There does seem to be evidence from the Basel sequence of a change in the distribution of events before and after shut-in of the injection well (Bachmann *et al.*, 2011). Here, we propose three tests for time-varying changes in the FMD of events and apply these to the Basel and Paralana seismic-

ity as example sequences that seem to show a change (Basel) and no change (Paralana). We are aware of selection bias in that we have already observed the largest event after shut-in at Basel. Future prospective tests will be needed to determine if this occurs at other locations.

The first test is to qualitatively detect a change in the distribution through time by plotting earthquake magnitudes versus event number (Fig. 12). For a time-invariant process, one would expect to see a uniform distribution of magnitudes versus event number. Qualitatively, the Basel sequence appears to have more large events at the end of the sequence, compared with a uniform distribution. The Paralana sequence appears qualitatively closer to uniform.

The second tests the null hypothesis that the observed maximum magnitude for the sequence is consistent with GR and the b-value estimated prior to shut-in; that is, that there is no change in the distribution between pre- and post shut-in. This is relevant to a forecasting scenario, in which it is of interest to forecast the largest magnitude given the rate of events and an initial estimate of the b-value. Given a b-value and observed number of events, van der Elst *et al.* (2016) derived the expression for the distribution on $M_{\max}$. Figure 13 shows the predicted mode and upper and lower 95% confidence bounds for a suite of b-values, together with distributions for b-value estimated using only events before shut-in (darker) and after shut-in (lighter). We used the Aki maximum-likelihood method to estimate b-values, and the distributions were generated using the bootstrap method. In this case, the observed $M_{\max}$ is not rejected at the 95% confidence level assuming the b-value prior to shut-in.

The third test for a change in the distribution is to determine whether or not the number of events above a certain magnitude threshold is consistent with the estimated b-value. For example, at Basel we can ask whether the number of events above a specified threshold observed after shut-in is
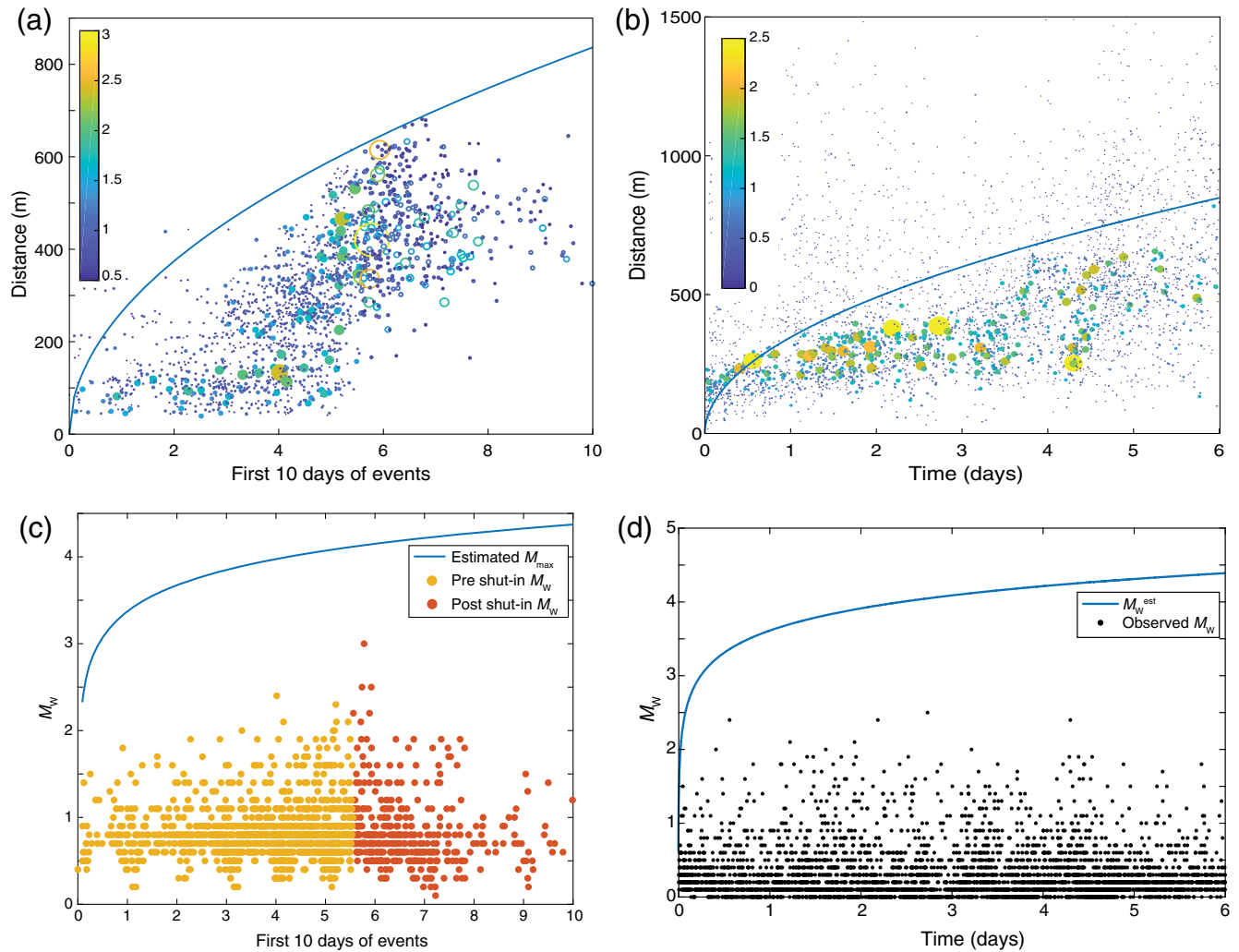
Figure 11. (a,b) Distance–time seismicity plots for Basel and Paralana. Dots show the observed seismicity, shaded by magnitude (size of dots also represents magnitude). Lines show an estimate of the perturbed radius in time based on fitting a diffusion curve of the form $a(t) = 2\sqrt{D_f t}$ to the seismicity cloud. (a) Basel seismicity, fit using $D_f = 0.202$ m/s^2. Solid circles occurred during injection, outlined circles occurred after shut-in. (b) Paralana seismicity, fit using $D_f = 0.347$ m/s^2. (c,d) Time evolution of M_{max} obtained by converting the estimated perturbed radius $a(t)$ to a magnitude using equation (A8), assuming $\Delta\tau = 3$ MPa for (c) Basel and (d) Paralana. The color version of this figure is available only in the electronic edition.

consistent with the b-value estimated before shut-in. To do this, we compute the probability distribution of observing N_M events equal to or above magnitude M, given the estimated b-value and the observed number of events. This distribution can be numerically simulated by generating sequences of events with magnitudes distributed according to GR (or any of the models discussed in this article) and tallying the number of events above the threshold in each sequence. Repeating this many times builds up an empirical distribution to compare with the observations. For GR, the distribution can also be analytically determined by first computing the probability that an event will be equal to or greater than a given magnitude:

$$P(m \geq M) = 10^{-b(M - M_c)}.$$

Then, the binomial probability density function gives the probability of observing N_M successes (i.e., magnitudes equal to or greater than M), out of N_e trials, in which N_e is the total number of events observed.

We apply this test to the Basel seismicity, in which $N_e = 182$ and $N_M = 7$ for $M = 2.5$, all of which occur after shut-in (Fig. 14). Predictions using the b-value estimated from seismicity before shut-in (Fig. 14a) and after shut-in (Fig. 14b) are compared with the observations. This test has the advantage of more statistical power than merely considering the single largest event size. Figure 14 shows that it is very unlikely for the distribution of events before shut-in to explain the events that occurred post shut-in. This evidence for a change in the FMD after shut-in supports the conclusion of Bachmann *et al.* (2011).
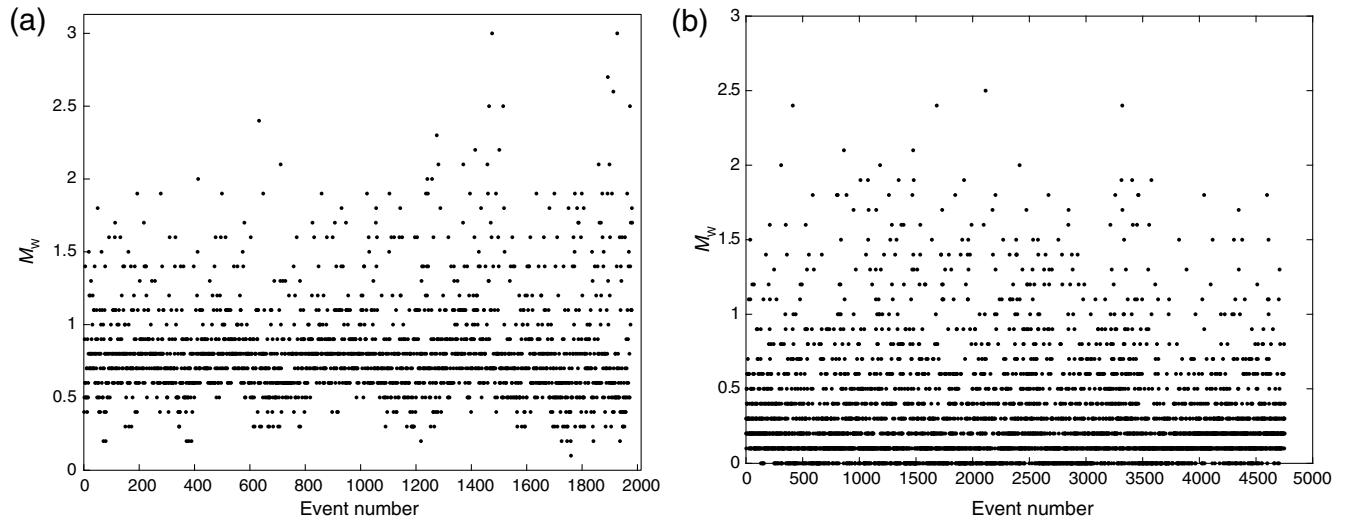
Figure 12. Earthquakes plotted by event number. (a) First year of the Basel Enhanced Geothermal System (EGS) seismicity; (b) Paralana EGS seismicity.

Conclusions

We analyzed a highly idealized model, consisting of (1) a spherical stress- and pore-pressure perturbed region, (2) earthquakes following a truncated GRD, and (3) applying the assumption that earthquake magnitudes are limited by the size of the perturbed region. We suggest that these approximations may be appropriate when the background shear to normal stress ratio is too low to allow self-sustained rupture.
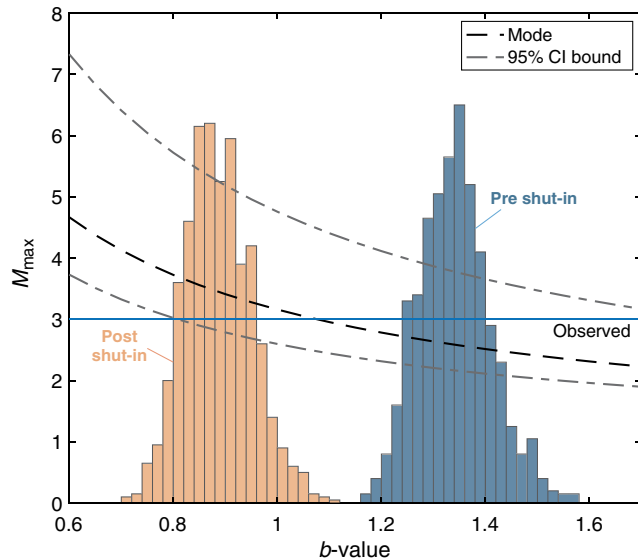
Figure 13. Expected versus observed $M_w^{(max)}$ assuming GR for the Basel sequence. Curving dashed lines are the mode and 95% confidence interval (CI) bounds for a range of b-values, computed using the expressions from van der Elst *et al.* (2016). Histograms are bootstrap-estimated probability density functions for b-value. Darker histogram is based on events prior to shut-in, lighter is post-shut-in events. The horizontal solid line is the observed M_{max}. The color version of this figure is available only in the electronic edition.

Results show interesting and even unexpected behavior in the relative frequencies of smaller and larger events during an injection sequence. Accounting for faults partially inside and fully covering the perturbed region increases the number of larger-magnitude events relative to the model in which faults must be fully within the perturbed volume, and in some cases even relative to the GRD. Time-dependent changes in the FMD are predicted that depend on the size of the perturbed region, total rate of events, maximum fault size, and b-value. The distribution rolls off at the largest possible magnitude, which grows in time as the perturbed region grows. The limiting distribution for $\rho_{max}/a(t) < 1$ is truncated GR. Even though the largest possible event grows in time, the largest observed event in any sequence will depend on the rate of events. The time-dependent changes in the FMD can lead to time-dependent changes in hazard from the largest expected events relative to GRD. Although the results presented here are highly idealized, they are rigorously derived and easily computed, allowing for easy testing against other data sets.

Data and Resources

Seismicity data for Basel are publicly available from Deichmann and Giardini (2009). Paralana data were provided to the authors by J. Albaric, relevant citation is Albaric *et al.* (2014). MATLAB codes to generate the plots shown in the figures in this article are freely available online in GitHub repository (www.github.com/jlmaurer/induced-seismicity-magnitudes, last accessed March 2018).

Acknowledgments
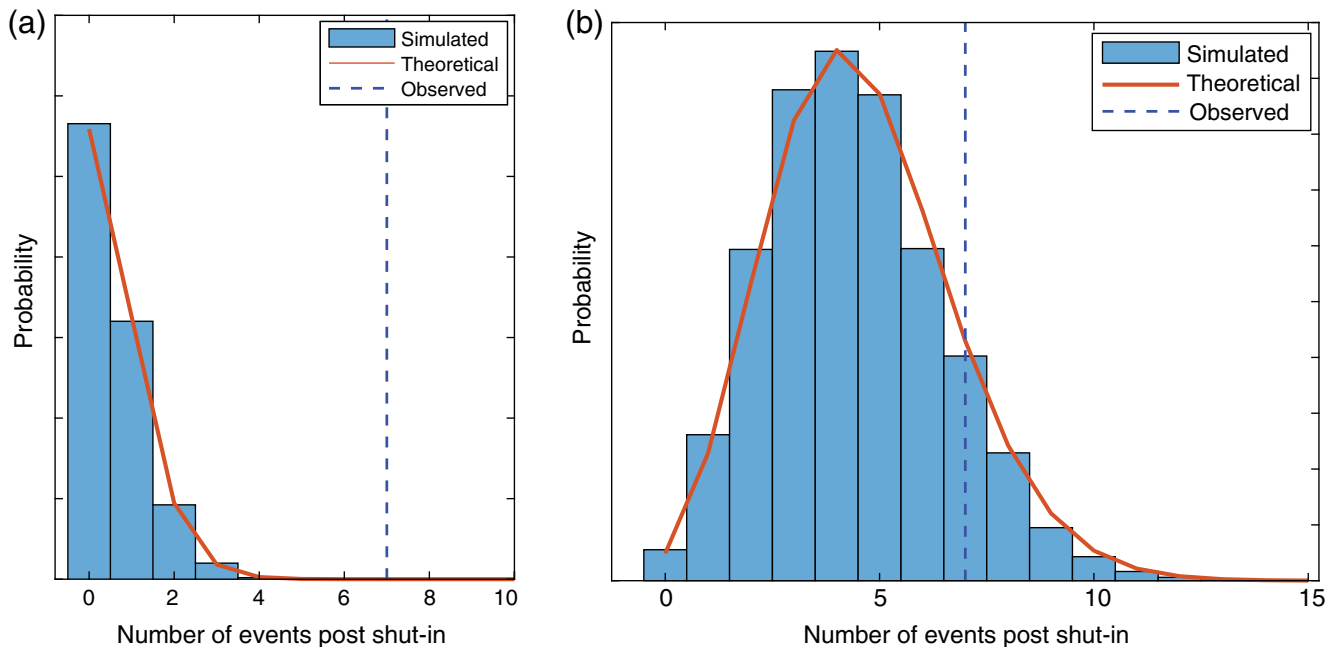
Figure 14. Probability distributions of observing $N_M = 7$ earthquakes of $M_w \geq 2.5$ post shut-in given the total number of events ($182 > M_c$). The distributions are simulated numerically (histograms) and computed theoretically (solid lines) using (a) b-value estimated using only events prior to shut-in ($= 1.56$); and (b) b-value estimated using only events post shut-in ($= 1$). The color version of this figure is available only in the electronic edition.

References

Albaric, J., V. Oye, N. Langet, M. Hasting, I. Lecomte, K. Iranpour, and P. Reid (2014). Monitoring of induced seismicity during the first geothermal reservoir stimulation at Paralana, Australia, *Geothermics* **52,** 120–131, doi: 10.1016/j.geothermics.2013.10.013.

Atkinson, G. M., H. Ghofrani, and K. Assatourians (2015). Impact of induced seismicity on the evaluation of seismic hazard: Some preliminary considerations, *Seismol. Res. Lett.* **86,** no. 3, 1009–1021, doi: 10.1785/0220140204.

Bachmann, C. E., S. Wiemer, J. Woessner, and S. Hainzl (2011). Statistical analysis of the induced Basel 2006 earthquake sequence: Introducing a probability-based monitoring approach for Enhanced Geothermal Systems, *Geophys. J. Int.* **186,** no. 2, 793–807, doi: 10.1111/j.1365-246X.2011.05068.x.

Baisch, S., R. Vörös, E. Rothert, H. Stang, R. Jung, and R. Schellschmidt (2010). A numerical model for fluid injection induced seismicity at Soultz-sous-Forêts, *Int. J. Rock Mech. Min. Sci.* **47,** no. 3, 405–413, doi: 10.1016/j.ijrmms.2009.10.001.

Deichmann, N., and D. Giardini (2009). Earthquakes induced by the stimulation of an Enhanced Geothermal System below Basel (Switzerland), *Seismol. Res. Lett.* **80,** no. 5, 784–798, doi: 10.1785/gssrl.80.5.784.

Dieterich, J. (1994). A constitutive law for rate of earthquake production and its application to earthquake clustering, *J. Geophys. Res.* **99,** no. B2, 2601–2618, doi: 10.1029/93JB02581.

Dieterich, J. H., K. B. Richards-Dinger, and K. A. Kroll (2015). Modeling injection-induced seismicity with the physics-based earthquake simulator RSQSim, *Seismol. Res. Lett.* **86,** no. 4, 1102–1109, doi: 10.1785/0220150057.

Dorbath, L., N. Cuenot, A. Genter, and M. Frogneux (2009). Seismic response of the fractured and faulted granite of Soultz-sous-Forets (France) to 5 km deep massive water injections, *Geophys. J. Int.* **177,** no. 2, 653–675, doi: 10.1111/j.1365-246X.2009.04030.x.

Dunham, E. M., D. Belanger, L. Cong, and J. E. Kozdon (2011). Earthquake ruptures with strongly rate-weakening friction and off-fault plasticity, part 1: Planar faults, *Bull. Seismol. Soc. Am.* **101,** no. 5, 2296–2307, doi: 10.1785/0120100076.

Fang, Z., and E. M. Dunham (2013). Additional shear resistance from fault roughness and stress levels on geometrically complex faults, *J. Geophys. Res.* **118,** no. 7, 3642–3654, doi: 10.1002/jgrb.50262.

Gel'fand, I. M., and G. E. Shilov (1964). Generalized functions, *Spaces of Fundamental and Generalized Functions*, Vol. 2, Academic Press, New York, New York.

Goertz-Allmann, B. P., A. Goertz, and S. Wiemer (2011). Stress drop variations of induced earthquakes at the Basel geothermal site, *Geophys. Res. Lett.* **38,** no. 9, doi: 10.1029/2011GL047498.

Hakimhashemi, A. H., M. Schoenball, O. Heidbach, A. Zang, and G. Grünthal (2014). Forward modelling of seismicity rate changes in georeservoirs with a hybrid geomechanical-statistical prototype model, *Geothermics* **52,** 185–194, doi: 10.1016/j.geothermics.2014.01.001.

Hanks, T. C., and H. Kanamori (1979). A moment magnitude scale, *J. Geophys. Res.* **84,** no. B5, 2348–2350, doi: 10.1029/JB084iB05p02348.

Kagan, Y. Y. (2002). Seismic moment distribution revisited: I. Statistical results, *Geophys. J. Int.* **148,** no. 3, 520–541, doi: 10.1046/j.1365-246x.2002.01594.x.

Kim, W.-Y. (2013). Induced seismicity associated with fluid injection into a deep well in Youngstown, Ohio, *J. Geophys. Res.* **118,** no. 7, 3506–3518, doi: 10.1002/jgrb.50247.

Király-Proag, E., J. D. Zechar, V. Gischig, S. Wiemer, D. Karvounis, and J. Doetsch (2016). Validating induced seismicity forecast models—Induced Seismicity Test Bench, *J. Geophys. Res.* **121,** no. 8, 6009–6029, doi: 10.1002/2016JB013236.

Kraft, T., and N. Deichmann (2014). High-precision relocation and focal mechanism of the injection-induced seismicity at the Basel EGS, *Geothermics* **52,** 59–73, doi: 10.1016/j.geothermics.2014.05.014.

Lay, T., and T. C. Wallace (1995). *Modern Global Seismology*, Vol. 58, Academic Press, San Diego, California.

McGarr, A. (2014). Maximum magnitude earthquakes induced by fluid injection, *J. Geophys. Res.* **119,** no. 2, 1008–1019, doi: 10.1002/2013JB010597.

McGarr, A., and A. Barbour (2017). Wastewater disposal and the earthquake sequences during 2016 Near Fairview, Pawnee, and Cushing, Oklahoma, *Geophys. Res. Lett.* **44,** no. 18, 9330–9336, doi: 10.1002/2017GL075258.

Richards-Dinger, K., R. S. Stein, and S. Toda (2010). Decay of aftershock density with distance does not indicate triggering by dynamic stress, *Nature* **467,** no. 7315, 583–586, doi: 10.1038/nature09402.

Schmitt, S. V., P. Segall, and E. M. Dunham (2015). Nucleation and dynamic rupture on weakly stressed faults sustained by thermal pressurization, *J. Geophys. Res.* **120,** no. 11, 7606–7640, doi: 10.1002/2015JB012322.

Segall, P., and S. Lu (2015). Injection-induced seismicity: Poroelastic and earthquake nucleation effects, *J. Geophys. Res.* **120,** no. 7, 5082–5103, doi: 10.1002/2015JB012060.

Shapiro, S. (2015). *Fluid-Induced Seismicity,* Cambridge University Press, Cambridge, United Kingdom.

Shapiro, S. A., O. S. Krüger, and C. Dinske (2013). Probability of inducing given-magnitude earthquakes by perturbing finite volumes of rocks, *J. Geophys. Res.* **118,** no. 7, 3557–3575, doi: 10.1002/jgrb.50264.

Shapiro, S. A., O. S. Krüger, C. Dinske, and C. Langenbruch (2011). Magnitudes of induced earthquakes and geometric scales of fluid-stimulated rock volumes, *Geophysics* **76,** no. 6, WC55–WC63, doi: 10.1190/geo2010-0349.1.

Tanizaki, H. (2004). *Computational Methods in Statistics and Econometrics,* Marcel Dekker, New York, New York.

van der Elst, N. J., M. T. Page, D. A. Weiser, T. H. Goebel, and S. M. Hosseini (2016). Induced earthquake magnitudes are as large as (statistically) expected, *J. Geophys. Res.* **121,** no. 6, 4575–4590, doi: 10.1002/2016JB012818.

Appendix

Correction to G_{stim} in Shapiro *et al.*

In this study, we presented the model of Shapiro *et al.* as given in their publications; however, one problem with this formulation is that the factor G_{stim} is not exactly correct as stated. This can be seen by integrating P_{event} over all fault sizes, which should be unity for a probability:

$$\int_{\rho_{min}}^{\rho_{max}} P_{event}(\rho)d\rho = \int_{\rho_{min}}^{\rho_{max}} \frac{P_s(\rho)}{P_c(\rho)}G(\rho)d\rho \neq 1,$$

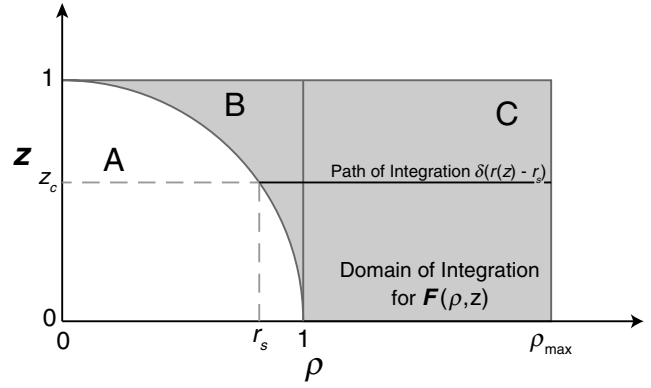which is most glaringly seen by setting $P_s = 1$ (the upper end-member model). Then

$$\int_{\rho_{min}}^{\rho_{max}} P_{event}(\rho)d\rho = \int_{\rho_{min}}^{\rho_{max}} \frac{G(\rho)}{P_c(\rho)}d\rho > 1,$$

because $P_c < 1$ for all $\rho > 0$. The correct expression for P_{event} under the assumptions of Shapiro *et al.* is then

$$P_{event}(\rho) = \frac{1}{C}P_s(\rho)\frac{G(\rho;b)}{P_c(\rho)}, \tag{A1}$$

in which C is a normalizing constant given by

$$C = C(\rho_{min}, \rho_{max}) = \int_{\rho_{min}}^{\rho_{max}} \frac{P_s(\rho)}{P_c(\rho)}G(\rho;b)d\rho.$$

Figure A1. Domain of integration for P_r (equation A2). The unit quarter-circle (domain A) is excluded from the integral. Domains B and C correspond to the integral bounds in equation (A2), and the delta function restricts the integral to $r(z) = \sqrt{1 - z^2} = r_s$ or $z = \sqrt{1 - r_s^2} = z_c$. This condition, given by the black horizontal line, is the integration path for a given z used to compute equations (A4) and (A5).

P_r for the 3D Case

Considering the third term in equation (11), we integrate over the domain $\rho > r(z)$ and $0 < r_c < \rho - r(z)$, which can be divided into regions B and C (shown in Fig. A1):

$$P_r(r_s) = \underbrace{\frac{1}{2}\int_0^1 \int_{\sqrt{1-z^2}}^1 (\rho - r(z))^2 \delta(r(z) - r_s)G(\rho)d\rho dz}_{\text{Domain B}}$$
$$+ \underbrace{\frac{1}{2}\int_0^1 \int_1^{\rho_{max}} (\rho - r(z))^2 \delta(r(z) - r_s)G(\rho)d\rho dz}_{\text{Domain C}}. \tag{A2}$$

Switching the order of integration is now relatively simple. We require the following identity for integrating a function convolved with the delta function

$$\int_{-\infty}^{\infty} F(x)\delta(g(x))dx = \sum_i \frac{F(x_i)}{|g'(x_i)|} \tag{A3}$$

(Gel'fand and Shilov, 1964), in which the prime indicates the derivative, and x_i are the roots of the function $g(x)$. From equation (A2), $F = F(\rho, z) = (\rho - \sqrt{1 - z^2})^2 G(\rho)$, $g(z) = \sqrt{1 - z^2} - r_s$, and $|g'(z)| = z/\sqrt{1 - z^2}$. $g(z)$ has two roots: $z_i = \pm\sqrt{1 - r_s^2} = \pm z_c$, but only the positive root applies here because the integration limits are from 0 to z_c. Therefore, we have $|g'(z_c)| = z_c/r_s$ and $F(\rho, z_c) = (\rho - r_s)^2 G(\rho)$.

Domain C is the simplest to compute, because the limits of integration are constant. Recalling the scaling $0 < r_s < 1$ gives

$$I_C = \frac{1}{2} \int_1^{\rho_{max}} G(\rho) \left[\int_0^1 (\rho - r(z))^2 \delta(r(z) - r_s) dz \right] d\rho$$

$$= \frac{1}{2} \frac{r_s}{z_c} \int_1^{\rho_{max}} (\rho - r_s)^2 G(\rho) d\rho \tag{A4}$$

The term for domain B is given by

$$I_B = \frac{1}{2} \int_{r_s}^1 G(\rho) \left[\int_{\sqrt{1-\rho^2}}^1 (\rho - r(z))^2 \delta(r(z) - r_s) dz \right] d\rho$$

$$= \frac{1}{2} \frac{r_s}{z_c} \int_{r_s}^1 (\rho - r_s)^2 G(\rho) d\rho \tag{A5}$$

Combining these two terms gives the final expression for:

$$P_r(r_s) = \frac{1}{2} \frac{r_s}{z_c} \int_{r_s}^{\rho_{max}} (\rho - r_s)^2 G(\rho) d\rho. \tag{A6}$$

Transforming Probability Distributions

The derivation in the main article requires the distribution of fault sizes $G(\rho; b)$. Although the general expression in equation (A26) does not require a Gutenberg–Richter distribution (GRD) of fault sizes, we will generally assume in this study that the background tectonic loading produces a (potentially truncated) GRD. Below we rederive expressions for transforming between the distribution on fault radius ρ and magnitude M_w. Our derivations are similar to those of Kagan (2002) and Shapiro (2015), although they handle slightly different cases of arbitrary stress drop (Shapiro, 2015) and bounded Gutenberg–Richter (Kagan, 2002).

Earthquake magnitudes and seismic moment are related by

$$M_w = (2/3) \log_{10}(M_0) - 6.03, \tag{A7}$$

in which M_0 is the moment in N · m (Hanks and Kanamori, 1979). Letting $\Delta\tau$ be stress drop, Δu slip, and μ be shear modulus, and assuming circular crack-like earthquake sources, we approximate M_0 as $\mu\Delta u\pi\rho^2$. Assuming $\Delta u \sim \Delta\tau\rho/c\mu$, in which $c = 7\pi/16$ is the geometrical factor for circular cracks (Lay and Wallace, 1995), equation (A7) becomes

$$M_w = (2/3) \log_{10}((\pi/c)\Delta\tau\rho^3) - 6.03. \tag{A8}$$

The GRD on magnitude is used to derive the corresponding distribution on fault radii. This is the background distribution of fault dimensions without consideration of perturbation induced by injection.

Given a map (function or transformation) between ρ and M_w, defined as $F : \rho \mapsto M_w$ with inverse transformation $F^{-1} : M_w \mapsto \rho$, the probability density function (PDF) for ρ can be found as

$$\phi(\rho) = \psi(F(\rho)) \left| \frac{dM_w}{d\rho} \right|, \tag{A9}$$

in which $\psi = G(\rho; b)$ is the GRD and ϕ is the corresponding distribution on ρ. F^{-1} is found from equation (A8):

$$\rho = F^{-1}(M_w) = \left[\frac{1}{((\pi/c)\Delta\tau)^{1/3}} 10^{(M_w + 6.03)/2} \right]. \tag{A10}$$

From Richards-Dinger et al. (2010), we have the PDF $\psi(M_w)$ assuming that $M_w^{(max)} \gg M_c$ (the magnitude of completeness)

$$\psi(M_w) = b \ln(10) 10^{-b(M_w - M_c)}, \tag{A11}$$

in which b is the b-value. Integrating this from M_c to ∞ gives

$$b \ln(10) \int_{M_c}^{\infty} 10^{-b(M_w - M_c)} dM_w = b \ln(10) \left[-\frac{10^{b(M_c - M_w)}}{b \ln(10)} \right]_{M_c}^{\infty}$$

$$= 1,$$

demonstrating that this is a PDF. The term $\left| \frac{dM_w}{d\rho} \right|$ reduces to

$$\left| \frac{dM_w}{d\rho} \right| = \left| \frac{d}{d\rho} ((2/3) \log_{10}(c\Delta\tau\pi\rho^3) - 6.03) \right| = \frac{2}{\ln(10)\rho}, \tag{A12}$$

in which we can neglect the absolute value sign because $\rho \geq 0$. Substituting equations (A8), (A11), and (A12) into equation (A9) leads to the PDF on fault radii

$$\phi(\rho) = \frac{2b}{\rho} 10^{-\frac{2b}{3}(\log_{10}((\pi/c)\Delta\tau\rho^3) - \log_{10}((\pi/c)\Delta\tau\rho_m^3))} = 2b \left(\frac{\rho_m^{2b}}{\rho^{2b+1}} \right), \tag{A13}$$

in which ρ_m is the minimum fault size, corresponding to the completeness threshold. The PDF on fault size $\phi(\rho)$ is thus given by a Pareto distribution with shape parameter $\alpha = 2b$ and scale parameter ρ_m.

To generate random samples from this distribution, note that

$$T = \frac{\rho_m}{U^{\frac{1}{2b}}}$$

is Pareto-distributed (Tanizaki, 2004, p. 133), in which U is a uniform random sample.

The final distribution on event radii r_s from equation (25) can be used to determine the distribution on magnitudes predicted by this study, using the forward mapping from ρ to M_w:

$$\psi_2(M_w) = \phi_2(G^{-1}(M_w)) \left| \frac{dr_s}{dM_w} \right|. \tag{A14}$$

Here, $\phi_2 = P(r_s)$ is the PDF for event radii (equation 25) and ψ_2 is the PDF for magnitude. (Here, we are incorporating the restriction to the perturbed region.) Taking the derivative of equation (A10) and transforming equation (25), we obtain the final posterior distribution on magnitude:

$$P(M_w) = P(r_s(M_w))\left[\frac{\ln(10)}{2((\pi/c)\Delta\tau)^{1/3}}10^{((1/2)(M_w+6.03))}\right]. \tag{A15}$$

Integration over ρ and Limit of Infinite Max Magnitude

Equation (25) in the main article gives the distribution on fault radii, taking into account the perturbed region. $G(\rho; b)$ the background fault distribution is given in equation (A13).

Substituting equation (A13) into equation (25) gives

$$P(r_s; b, \rho_{max}) = \frac{\kappa}{2}(2b\rho_m^{2b})\left[z_c - r_s\cos^{-1}(r_s) - \frac{z_c^3}{3}\right](r_s^{-2b-1})$$
$$+ \kappa(2b\rho_m^{2b})\int_{r_s}^{\rho_{max}}[\cos^{-1}(r_s) + (2\rho - 3r_s)z_c](\rho^{-2b-1})d\rho$$
$$+ \frac{\kappa}{2}(2b\rho_m^{2b})\frac{r_s}{z_c}\int_{r_s}^{\rho_{max}}(\rho - r_s)^2(\rho^{-2b-1})d\rho. \tag{A16}$$

The first integral can be simplified and computed directly

$$\int_{r_s}^{\rho_{max}}[\cos^{-1}(r_s) + (2\rho - 3r_s)z_c](\rho^{-2b-1})d\rho$$
$$= [\cos^{-1}(r_s) - 3z_c r_s]\int_{r_s}^{\rho_{max}}(\rho^{-2b-1})d\rho + 2z_c\int_{r_s}^{\rho_{max}}\rho^{-2b}d\rho$$
$$= \left[\frac{3z_c r_s}{2b} - \frac{\cos^{-1}(r_s)}{2b}\right](\rho_{max}^{-2b} - r_s^{-2b}) + \frac{2z_c}{1-2b}(\rho_{max}^{-2b+1} - r_s^{-2b+1})$$
$$= \left(\frac{\rho_{max}^{-2b}}{2b}\right)\gamma_b(\rho_{max}) - \left(\frac{r_s^{-2b}}{2b}\right)\gamma_b(r_s), \tag{A17}$$

in which

$$\gamma_b(x) = -\cos^{-1}(r_s) + z_c\frac{4b}{1-2b}x + 3z_c r_s, \qquad x \in \{r_s, \rho_{max}\}.$$

If $b = 1$, the integral becomes

$$\left(\frac{\rho_{max}^{-2}}{2}\right)[-\cos^{-1}(r_s) - 4z_c\rho_{max} + 3z_c r_s]$$
$$+ \left(\frac{r_s^{-2}}{2}\right)[\cos^{-1}(r_s) + z_c r_s]. \tag{A18}$$

For the second integral in equation (A16), it is necessary to distinguish between $b < 1$, $b = 1$, and $b > 1$. If $b \leq 1$, the integral only converges for finite ρ_{max}, whereas for $b > 1$, the

integral converges even when $\rho_{max} \to \infty$. So the GRD does not decay sufficiently rapidly to allow the maximum fault size to go to infinity when $b \leq 1$.

Evaluating the second integral for $b > 1$

$$\int_{r_s}^{\rho_{max}}(\rho^2 - 2\rho r_s + r_s^2)(\rho^{-2b-1})d\rho$$
$$= \left(\frac{\rho_{max}^{-2b}}{2b}\right)\gamma_b'(\rho_{max}) - \left(\frac{r_s^{-2b}}{2b}\right)\gamma_b'(r_s), \tag{A19}$$

in which

$$\gamma_b'(x) = \frac{b}{1-b}x^2 - \frac{4br_s}{1-2b}x - r_s^2, \qquad x \in \{r_s, \rho_{max}\}.$$

For $b = 1$

$$= \int_{r_s}^{\rho_{max}}(\rho^{-1} - 2\rho^{-2}r_s + \rho^{-3}r_s^2)d\rho$$
$$= -\ln\left(\frac{r_s}{\rho_{max}}\right) - \frac{1}{2}\left(\frac{r_s}{\rho_{max}}\right)^2 + 2\frac{r_s}{\rho_{max}} - \frac{3}{2}. \tag{A20}$$

Now, the solutions for each integral above (for the appropriate values for b) can be substituted into equation (A16). Doing this for $b > 1$ gives

$$\frac{2}{\kappa}P(r_s; b > 1, \rho_{max}, \rho_m)$$
$$= \left(\frac{2b}{\rho_m^{-2b}}\right)\left[z_c - r_s\cos^{-1}(r_s) - \frac{z_c^3}{3}\right](r_s^{-2b-1})$$
$$+ 2\left(\frac{2b}{\rho_m^{-2b}}\right)\left[\left(\frac{\rho_{max}^{-2b}}{2b}\right)\gamma_b(\rho_{max}) - \left(\frac{r_s^{-2b}}{2b}\right)\gamma_b(r_s)\right]$$
$$+ \left(\frac{2b}{\rho_m^{-2b}}\right)\frac{r_s}{z_c}\left[\left(\frac{\rho_{max}^{-2b}}{2b}\right)\gamma_b'(\rho_{max}) - \left(\frac{r_s^{-2b}}{2b}\right)\gamma_b'(r_s)\right]. \tag{A21}$$

Rearranging the first line gives

$$\left(\frac{r_s}{\rho_m}\right)^{-2b}2b\left[z_c - r_s\cos^{-1}(r_s) - \frac{z_c^3}{3}\right]r_s^{-1}$$
$$= \left(\frac{r_s}{\rho_m}\right)^{-2b}\left[\frac{2b}{3}\frac{z_c}{r_s}(2 + r_s^2) - 2b\cos^{-1}(r_s)\right]$$
$$= \left(\frac{r_s}{\rho_m}\right)^{-2b}(2\Gamma_b(r_s)).$$

Then

$$\frac{2}{\kappa} P(r_s; b > 1, \rho_{\max}, \rho_m) = \left(\frac{r_s}{\rho_m}\right)^{-2b} 2\Gamma_b(r_s)$$

$$+ 2\left(\frac{\rho_{\max}}{\rho_m}\right)^{-2b} \gamma_b(\rho_{\max}) - 2\left(\frac{r_s}{\rho_m}\right)^{-2b} \gamma_b(r_s)$$

$$+ \left(\frac{\rho_{\max}}{\rho_m}\right)^{-2b} \frac{r_s}{z_c} \gamma'_b(\rho_{\max}) - \left(\frac{r_s}{\rho_m}\right)^{-2b} \frac{r_s}{z_c} \gamma'_b(r_s). \quad \text{(A22)}$$

Gathering terms and simplifying, the final solution can then be written as

$$P(r_s; b > 1, \rho_{\max}, \rho_m)$$

$$= \kappa \left[\left(\frac{r_s}{\rho_m}\right)^{-2b} F_b(r_s) + \left(\frac{\rho_{\max}}{\rho_m}\right)^{-2b} H_b(r_s; \rho_{\max}) \right], \text{(A23)}$$

in which for $b > 1$

$$F_b(r_s) = \Gamma_b(r_s) - \gamma_b(r_s) - \frac{r_s}{2z_c} \gamma'_b(r_s)$$

$$= \frac{b}{3} z_c \frac{(2 + r_s^2)}{r_s} + (1 - b) \cos^{-1}(r_s) + \left(\frac{2b - 3}{1 - 2b}\right) z_c r_s$$

$$+ \frac{r_s^3}{2z_c} \left(\frac{1}{(1 - b)(1 - 2b)}\right) \quad \text{(A24)}$$

and

$$H_b(r_s; \rho_{\max}) = \gamma_b(\rho_{\max}) + \frac{r_s}{2z_c} \gamma'_b(\rho_{\max})$$

$$= -\cos^{-1}(r_s) + \frac{r_s}{2z_c} \left[\frac{b}{1 - b} (\rho_{\max})^2 + \frac{(2 - 3r_s^2)}{r_s} \right.$$

$$\left. \frac{4b}{1 - 2b} \rho_{\max} + (6 - 7r_s^2) \right]. \quad \text{(A25)}$$

Taking the limit as $\rho_{\max} \to \infty$, the second term in the brackets in equation (A23) vanishes, leaving only

$$P(r_s; b > 1, \rho_{\max} \to \infty) = \kappa \left(\frac{r_s}{\rho_m}\right)^{-2b} F_b(r_s). \quad \text{(A26)}$$

For $b = 1$, substituting equations (A18) and (A20) into equation (A16) gives

$$P(r_s; b = 1, \rho_{\max})$$

$$= \kappa \left(\frac{r_s}{\rho_m}\right)^{-2} [\Gamma_1(r_s) + F_1(r_s; \rho_{\max}) + H_1(r_s; \rho_{\max})],$$

$$\text{(A27)}$$

in which for $R = r_s / \rho_{\max}$

$$\Gamma_1 = \frac{z_c}{3r_s} (2 + r_s^2) - \cos^{-1}(r_s),$$

$$F_1(r_s; \rho_{\max}) = [(\cos^{-1}(r_s) - 3r_s z_c)(1 - R^2) + 4z_c r_s(1 - R)]$$

and

$$H_1(r_s; \rho_{\max}) = \frac{r_s^3}{z_c} \left[-\ln(R) - \frac{1}{2}(R)^2 + 2R - \frac{3}{2} \right].$$

Department of Geophysics
Stanford University
397 Panama Mall
Mitchell Building 101, 3rd Floor
Stanford, California 94305
jlmaurer@stanford.edu